Chapter 4. Analysis and Measurement of Star Spiral Antenna

The star spiral is a type of slow-wave spiral developed to bridge the performance gap in the linear WAVES array detailed in the previous chapter. The linear WAVES array has a gap in coverage between the appearance of grating lobes at the end of the first octave and satisfactory VSWR performance of the second octave antenna element. The benefit of the star spiral is twofold. The slow-wave nature of the star spiral reduces the low frequency cutoff for the spiral and the unique shape of the star spiral allows for tighter array packing. Variations of the star spiral and a genetic algorithm optimization of the star spiral will be presented. Furthermore, measurements and simulations will show a favorable comparison between the star spiral and a circular Archimedean spiral.

4.1 Evolution of Star Spiral

A standard complementary Archimedean spiral is shown in Fig. 4.1. The spiral parameters are as follows: $r_2 = 0.05m$, $N = 16$ turns, and $segments = 40/turn$ for simulation. The results for a circular Archimedean spiral were presented in Chapter 2 and they are shown again here for ease of comparison to the various slow-wave spirals to be studied in this section. Once again, NEC4 is used to simulate all of the spiral antenna elements.

Initial attempts at producing a slow-wave spiral used the standard zigzag profile as shown in Fig. 4.2. The specifications for the zigzag spiral are $r_2 = 0.05m$, $N = 16$ turns, $segments = 40/turn$, and $dr = 7\times10^{-6}\,m$. The parameter dr represents the change in radius of the spiral from circular. The zigzag spiral was created by alternately adding and subtracting from the circular profile of Fig. 4.1 as follows:

$$\rho = \begin{cases} \rho + dr \times segment\#, & segment\# \rightarrow even \\ \rho - dr \times segment\#, & segment\# \rightarrow odd \end{cases} \tag{4.1}$$

The path for each arm of the spiral in polar coordinates is described by ρ and the total number of segments is given by $N \times seg/turn = 16 \times 40 = 640 segments$. So, $dr \times segment\#$ increases as the distance from the center of the spiral increases, creating

an ever-increasing zigzag profile. Many other zigzag profiles were also simulated with similar results to those of the zigzag spiral in Fig. 4.2. A constant zigzag profile, only modifying the even numbered segments, and starting the zigzag profile at some distance from the center have all been examined.

Other, lower frequency zigzag or star shaped, profiles as in Fig. 4.3 were also simulated. To create the spiral of Fig. 4.3, the number of segments was reduced to 16/turn and the star shape was determined by adding to the circular profile at even number segments,

$$\rho = \begin{cases} \rho + dr \times segment\#, & segment\# \rightarrow even \\ \rho, & segment\# \rightarrow odd \end{cases} \tag{4.2}$$

The pointed star spiral parameters are $r_2 = 0.05m$, $N = 16$ turns, $segments = 16/turn$, and $dr = 1.35 \times 10^{-4} m$. A potential advantage of the pointed star spiral is in array packing where the tip of one spiral can be interleaved with a valley of an adjacent spiral. The spirals of Fig. 4.2 and Fig. 4.3 are representative of the two main types of slow-wave spirals. The zigzag spiral of Fig. 4.2 is still essentially circular with the profile added to increase the outer circumference of the spiral. The star shaped spiral of Fig. 4.3 also has an increased circumference, but the spiral is really no longer circular in nature.

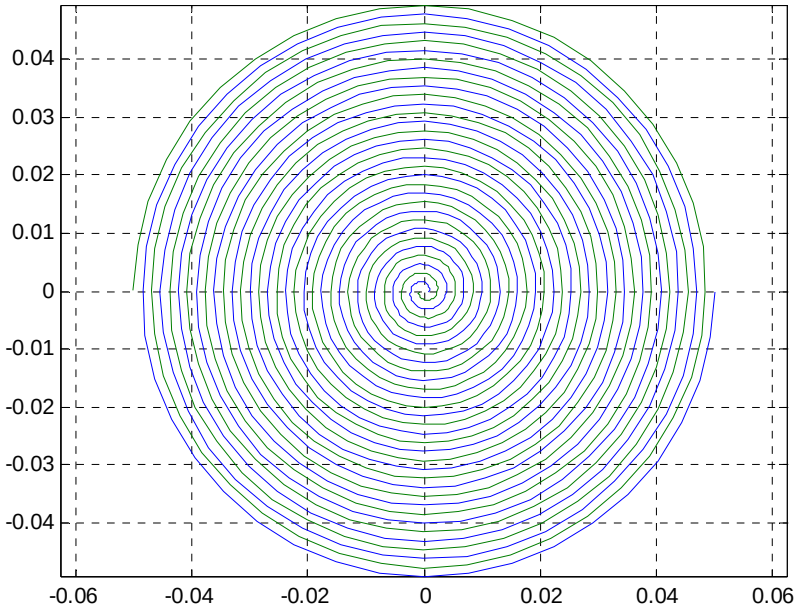

Figure 4.1 Complementary circular Archimedean spiral.

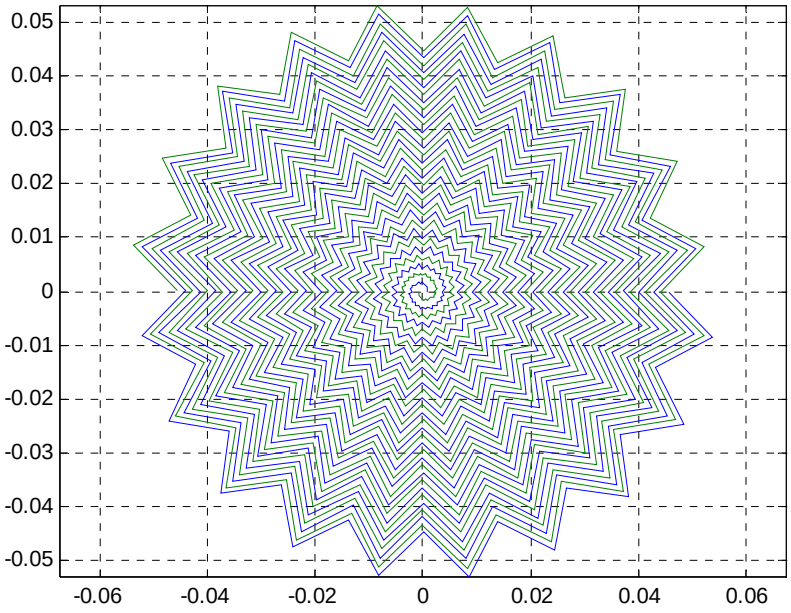

Figure 4.2 Slow-wave spiral with zigzag profile.

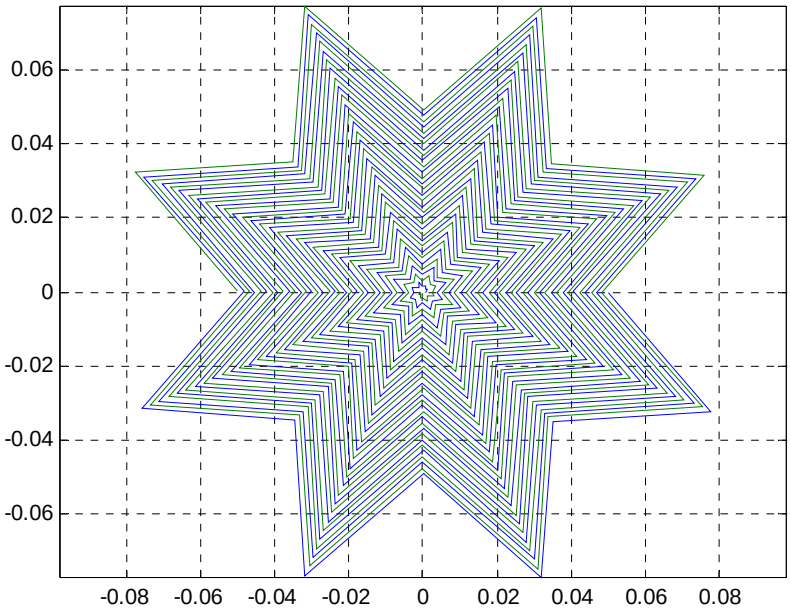

Figure 4.3 Slow-wave spiral with star shaped profile.

The VSWR, gain, and axial ratio results for the two slow-wave spirals are compared with the circular spiral in Fig. 4.4, Fig. 4.5, and Fig. 4.6, respectively. The low frequency cutoff and the length of the last turn of each spiral are summarized in Table 4.1. Note that the percent improvements are compared to the circular spiral standard. Theoretically, the low frequency cutoff of a spiral antenna is found when the length of the last turn of the spiral equals one wavelength, as in (2.9). So, the improvement in low frequency cutoff should correlate to the increase in the length of the last turn of the spiral. Table 4.1 shows that for the zigzag spiral a much larger reduction in the low frequency cutoff is expected based on the increase in length of the last turn. For the pointed star spiral, the low frequency cutoff actually increases, but its last turn length is more than double the last turn length of the circular spiral. Also, from Fig. 4.4 it's apparent that the VSWR for the pointed star spiral is not very stable and it gets worse as dr is increased. Furthermore, the gain for both the zigzag spiral and the pointed star spiral, as seen in Fig. 4.5, is significantly less than the gain of the circular spiral. This is due to the opposing currents created by both the zigzag and pointed star slow-wave profiles. The axial ratio, shown in Fig. 4.6, for the zigzag spiral is slightly worse than that of the circular spiral, particularly between 1000 MHz and 1500 MHz. The axial ratio of the pointed star spiral is acceptable below 2500 MHz, but then begins to break down with increasing frequency.

Table 4.1 Comparison of circular and slow-wave spiral performance.

Spiral Antenna Element	Low frequency cutoff, [MHz]	% Improvement in low frequency cutoff	Length of last turn, [m]	% Increase in length of last turn
Circular	1010	—	0.3042	—
Zigzag	895	11.4%	0.4612	51.6%
Pointed Star	1385	-37.1%	0.6666	119.1%

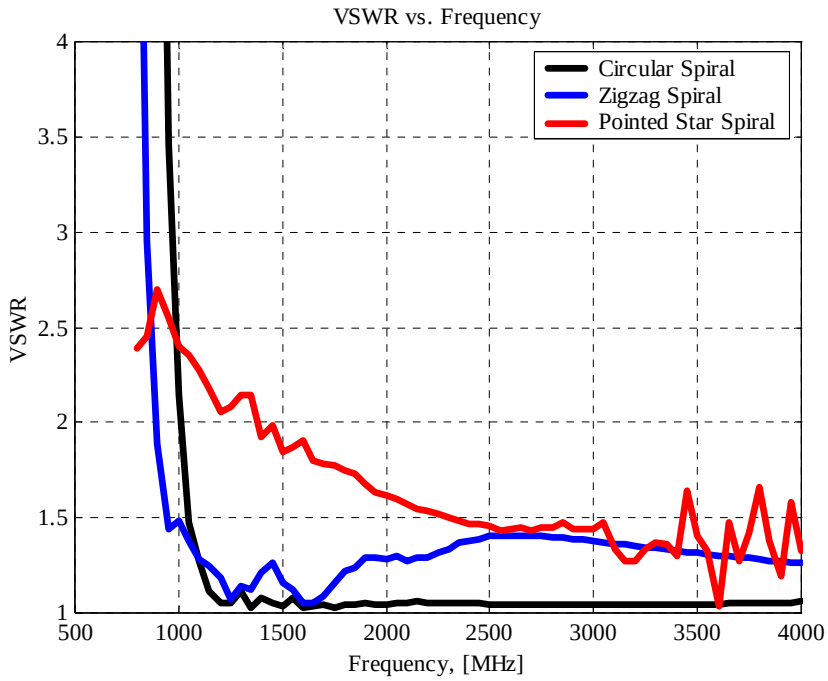

Figure 4.4 Comparison of VSWR for circular, zigzag, and pointed star spirals

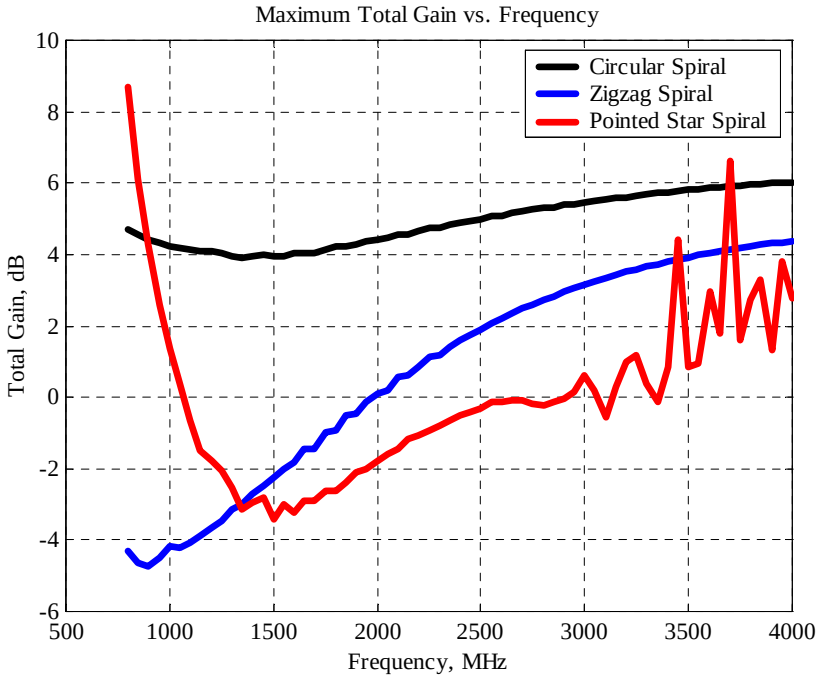

Figure 4.5 Comparison of gain for circular, zigzag, and pointed star spirals.

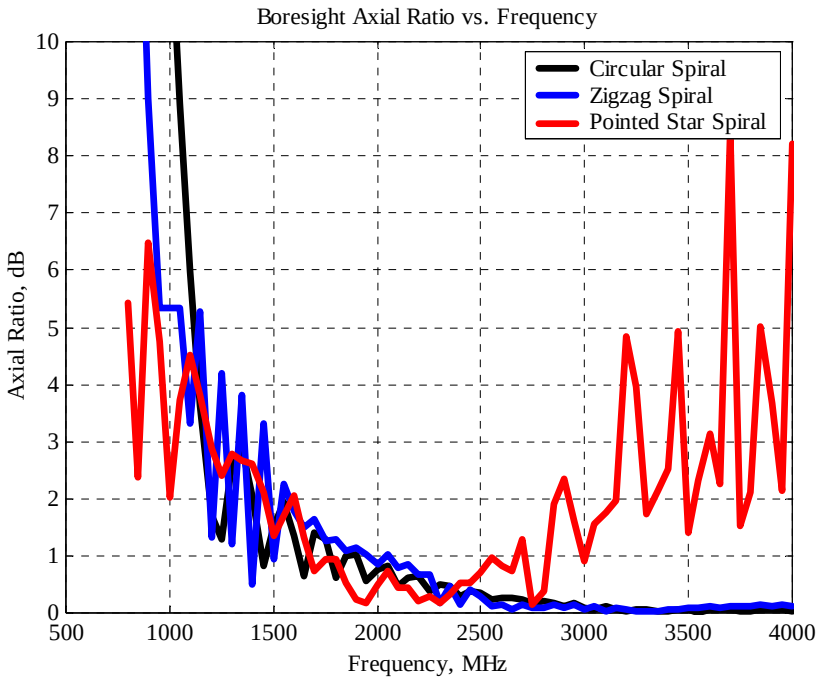

Figure 4.6 Comparison of axial ratio for circular, zigzag, and pointed star spirals.

The reduction in element gain seen in Fig. 4.5 for the slow-wave spirals necessitated further modifications to the slow-wave spiral before it may be used in a WAVES array. A variation of the pointed star spiral was developed with the points flattened out. The goal was to reduce the gain loss by minimizing the opposing currents seen in the pointed star spiral. The result of the first iteration of the star spiral antenna element is shown in Fig. 4.7 with parameters $r_2 = 0.038m$, $N = 16$ turns, $dr = 8.9\times10^{-5}$, $v = 0$, and $segments = 16/turn$. The parameter v determines where the star spiral starts or how much of the center of the spiral is purely circular. The star spiral was further improved by using a circular center in the star spiral as in Fig. 4.8. The specs for the spiral of Fig. 4.8 are $r_2 = 0.038m$, $N = 16$ turns, $dr = 1.43\times10^{-4}$, $v = 24$, and $segments = 16/turn$. The star spiral is based on the 4 segment repeating pattern described below,

$$\rho = \begin{cases} \rho + dr \times segment\# & segments \rightarrow 2\,\&\,3 \\ \rho & segments \rightarrow 1\,\&\,4 \end{cases} \tag{4.3}$$

Also, in (4.3) the segment number is bounded by $4v \le segment\# \le total\ segments$ providing for the circular center when $v > 0$.

The VSWR, gain, and axial ratio for both star spirals and, for comparison, the circular spiral is shown in Fig. 4.9, Fig. 4.10, and Fig. 4.11, respectively. Furthermore, the low frequency cutoffs and last turn lengths are summarized in Table 4.2. Both star spiral iterations exhibit approximately an 11% reduction in low frequency cutoff compared to a 24% increase in last turn length. There is still a smaller size reduction than expected but the performance is greatly improved over the zigzag spiral and pointed star spiral. The VSWR for the first star spiral is below 2:1 but the fluctuations with frequency are a concern. This problem has been addressed by using a circular center, which smoothes out the VSWR performance, particularly at higher frequencies, and also reduces the variation in the gain curves.

The gain loss observed for the zigzag spiral and pointed star spiral has also been improved with the star spiral. The gain of the star spiral is on average within 1dB of the gain predicted for the circular Archimedean spiral.

The axial ratio of the star spiral with the circular center is approximately 3dB on average, but exceeds 3dB at many points in the frequency band. An axial ratio of less than 3dB is required for acceptable circular polarization, so the star spiral with the circular center is borderline at best in terms of polarization performance. The axial ratio of the star spiral is unacceptable over most of the frequency range, but it can be improved by using a 4-arm star spiral antenna. Also, the frequency range has been extended up to 8GHz to accommodate the design of three-octave WAVES arrays in Chapter 6.

Table 4.2 Comparison of star spiral and circular spiral performance.

Spiral Antenna Element	Low frequency cutoff, [MHz]	% Improvement in low frequency cutoff	Length of last turn, [m]	% Increase in length of last turn
Circular	1010	—	0.3042	—
Star Spiral	903	10.6%	0.3786	24.5%
Star with circular center	892	11.7%	0.3760	23.6%

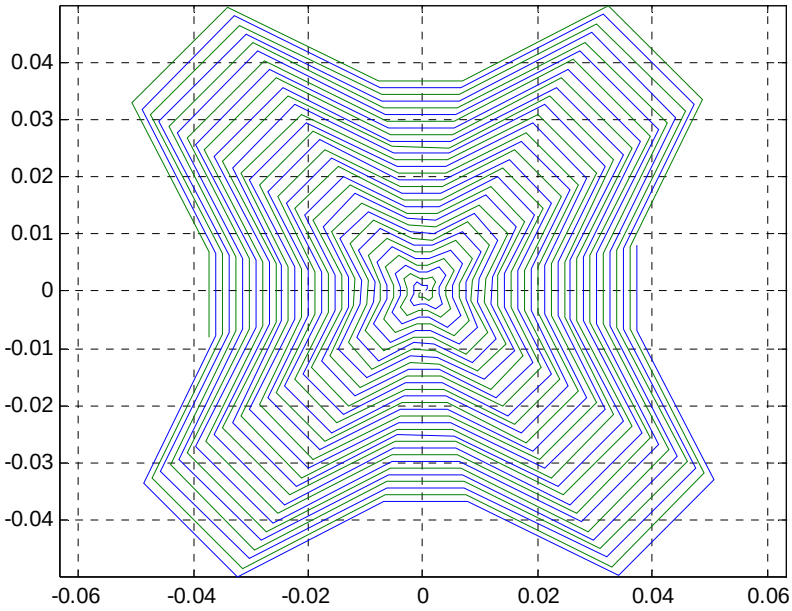

Figure 4.7 First iteration star spiral antenna element.

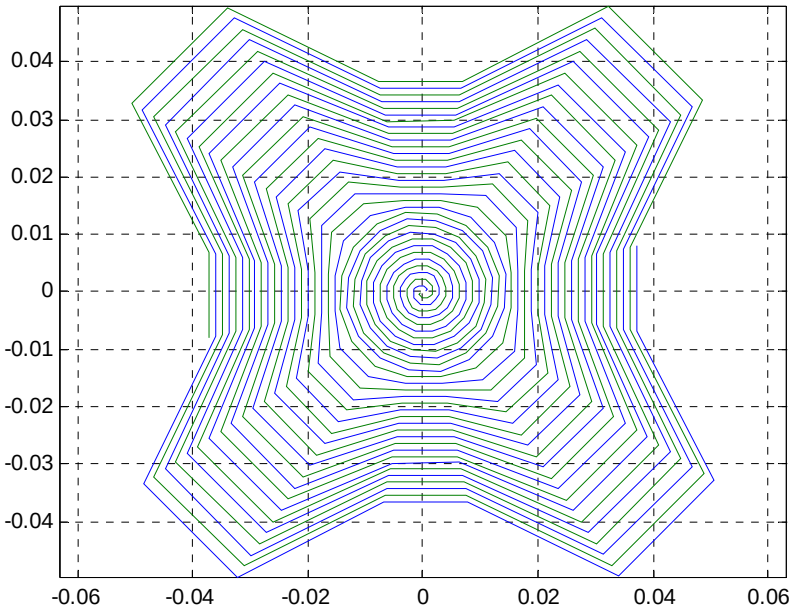

Figure 4.8 Star spiral with circular center.

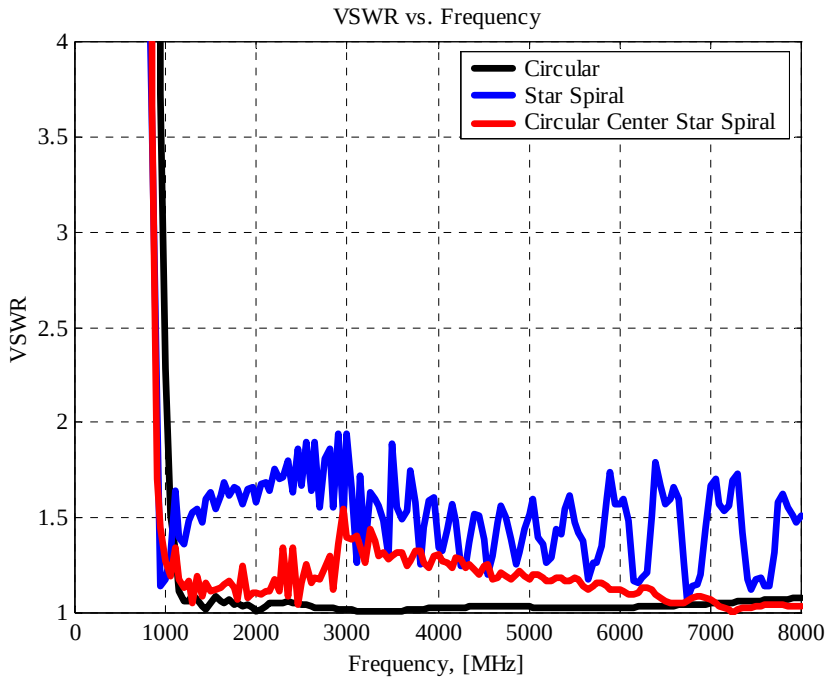

Figure 4.9 Comparison of VSWR for two star spiral antennas and circular spiral.

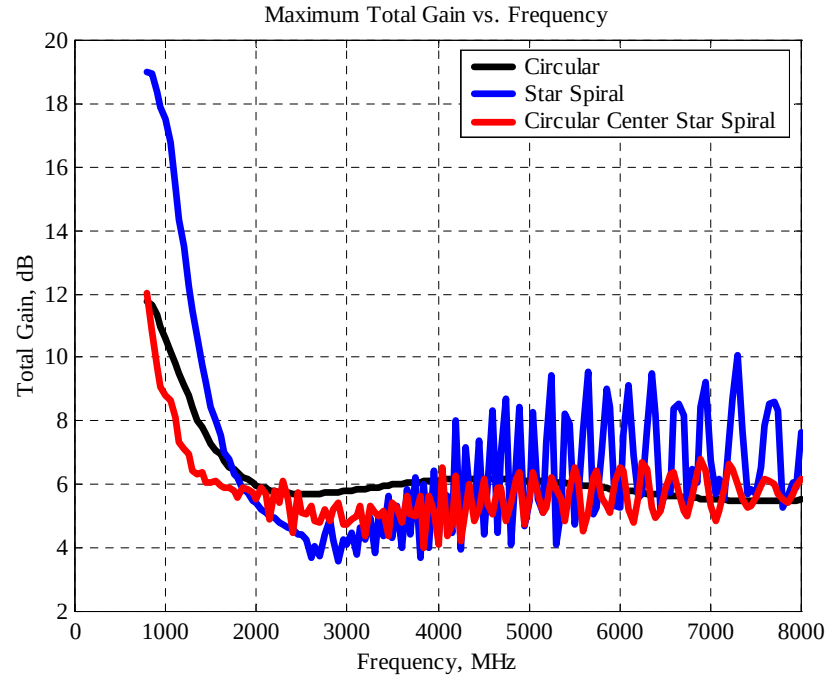

Figure 4.10 Comparison of gain for two star spiral antennas and circular spiral.

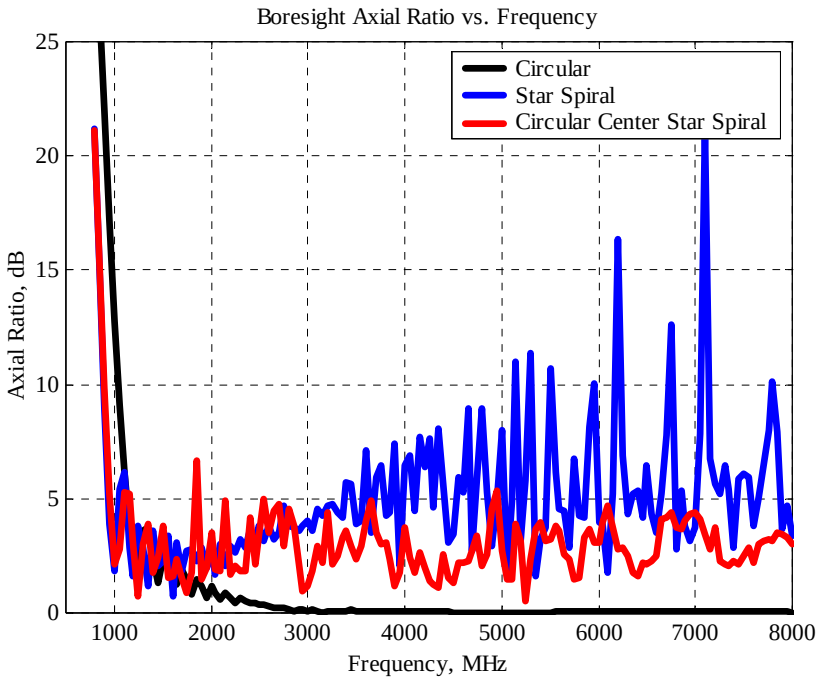

Figure 4.11 Comparison of axial ratio for two star spiral antennas and circular spiral.

4.2 Star Spiral Optimization With Genetic Algorithm

The genetic algorithm is becoming popular for optimizing antenna problems due to its versatility. The genetic algorithm is often used to solve problems where the antenna structure is unknown. For example, the genetic algorithm has been used to optimize a wire antenna constrained to fit inside a cube of specified size. The number, size, and connection of wires inside the cube are determined by the genetic algorithm. Criticism of the genetic algorithm originates in examples as described above where basic antenna principles are not used in the design process. In this dissertation the genetic algorithm will be used to optimize a spiral antenna. The basic antenna structure is known, but parameters such as number of turns, antenna diameter, and expansion ratio will be optimized. Additional parameters will also be optimized when considering the star spiral.

The basics of the genetic algorithm (GA) have been presented in many books and articles, so only the specific type of GA used in this dissertation will be briefly described (Johnson and Rahmat-Samii, 1997, Vose, 1999). The parameters of interest are converted into binary numbers called genes. All of the genes are combined into a single binary number called a chromosome. The initial population is randomly generated.

NEC4 is used to evaluate each chromosome by converting each gene of the chromosome into its decimal equivalent and creating a NEC4 input file. Parameters such as frequency, number of segments, feed location, and radiation pattern specifications are set before the GA is started. The NEC4 output file is then evaluated to determine the performance of each chromosome. The exact cost function will be detailed later, but the general procedure was to rank each chromosome by low frequency cutoff. The lower the frequency where the VSWR exceeded 2:1 the better the chromosome was ranked.

After each generation was evaluated, the top 50% of the chromosomes were kept and used to create the other 50% of the next generation. The next generation was created by randomly picking a crossover point for each chromosome and the new chromosome was formed by matching the first part of one chromosome with the second part of the next chromosome. Mutation was also included by randomly picking a chromosome to mutate and then randomly picking the bit in the chromosome to mutate. The highest-ranking chromosome was never mutated. Typically, the genetic algorithm was run through a set number of generations in an attempt to find the spiral with the best low frequency cutoff.

The first attempt at optimizing the star spiral started from a fixed outer radius, $r_2 = 0.03149m$, and number of turns, $N = 7$. The parameters that were optimized were the circular offset, dr, amount of circular center, v, and the expansion exponent, $taper$. The expansion exponent controls how tightly the spiral is wound and was added to provide a smoother transition from the circular center to the outer star shape. The star spiral follows the equation

$$\rho = \begin{cases} \rho + \left(dr \times segment\#\right)^{segment\#/\,taper} & segments \rightarrow 2\ \&\ 3 \\ \rho & segments \rightarrow 1\ \&\ 4 \end{cases} \tag{4.4}$$

where once again the segment number is bounded by $4v \le segment\# \le total\ segments$ to provide for the circular center. The cost function for this optimization was to find the minimum VSWR at 1100MHz. The genetic algorithm returned a star spiral with $dr = 0.00031$, $v = 7$, and $taper = 110$. The spiral is plotted in Fig. 4.12. The VSWR for

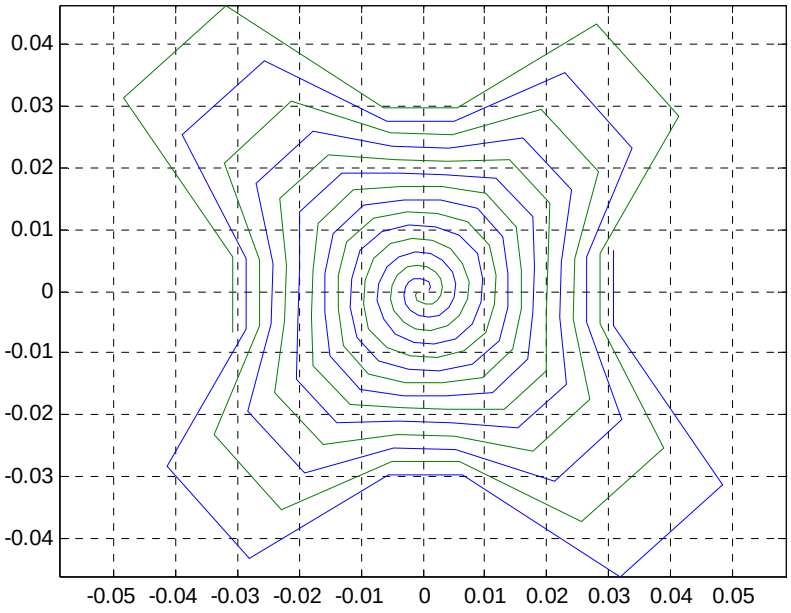

Figure 4.12 Result of first genetic algorithm optimization.

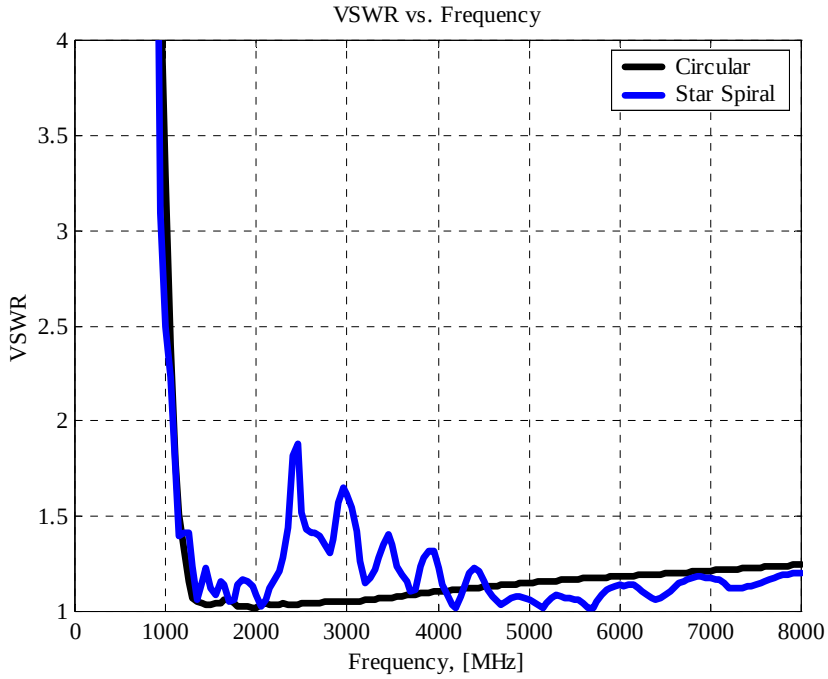

Figure 4.13 VSWR comparison for circular spiral and result of first genetic algorithm optimization (Fig. 4.12).

the star spiral of Fig. 4.12 is plotted in Fig. 4.13 along with the VSWR for an equivalent circular spiral. The equivalent circular spiral has the same linear extent and number of turns as the star spiral so both spirals would occupy the same space in a linear array. This method of determining the equivalent circular spiral will be used throughout the remainder of this dissertation. So, the circular spiral as an outer radius of $r_2 = 0.0484m$ and $N = 7$ turns. The star spiral of Fig. 4.12 has a last turn circumference of 0.3195m and a low frequency cutoff 1074MHz, and the equivalent circular spiral has a last turn circumference of 0.2814m with a low frequency cutoff of 1083MHz. The star spiral provides a 13.5% increase in circumference but only a 0.8% improvement in the low frequency cutoff. The lack of size reduction found in the star spiral of Fig. 4.12 can be attributed to a smaller increase in last turn circumference compared to the star spirals listed in Table 4.2, which have about a 24% improvement in circumference compared to their equivalent circular spiral. Redefining the problem statement and refining the cost function should improve the results of the genetic algorithm.

The second iteration of the genetic algorithm was the same as the previous example with one new parameter. The *trans* parameter, defines a transition region between the circular center of the spiral and the purely star shaped outer turn of the star spiral. The *taper* parameter now is only used in the transition region. This new formulation should allow for the improved circumference seen in Table 4.2 and a more stable VSWR across the band. The outer radius, $r_2 = 0.03149m$, the number of turns, $N = 7$, and the cost function of minimum VSWR at 1100MHz are all the same as the first GA run. Also, a circular offset of $dr = 0.0003$ and a circular center of $v = 8$ was used in this example. Since the outer shape of the spiral is fixed for this example, the goal was to find the spiral with best size reduction for a given last turn circumference and also to minimize fluctuations in the VSWR.

The spiral is formed using the following equation

$$\rho = \begin{cases} \rho + \left(dr \times segment\#\right)^{segment\#/\,taper} & 4v \le segment\# \le trans \\ \rho + dr \times segment\# & segment\# > trans \end{cases} \tag{4.5}$$

for segments 2 and 3 and ρ is unchanged for segments 1 and 4 as usual. The results of the second GA run are $taper = 113$ and $trans = 5$, and the spiral is shown in Fig. 4.14.

The star spiral of Fig. 4.14 has a last turn circumference of 0.3375m, an effective radius of 0.0458m, and a low frequency cutoff of 992MHz. The effective radius of the star spiral is the radius of a circular spiral that has the same linear extent as the star spiral. The VSWR for the star spiral and its equivalent circular spiral is shown in Fig. 4.15. The star spiral of Fig. 4.14 shows a 26.7% improvement in last turn circumference and a 12.6% reduction in low frequency cutoff compared to the equivalent circular spiral. The results of the second GA run show a significant improvement in size reduction compared to the first run but the oscillations in the VSWR plot is still a concern.

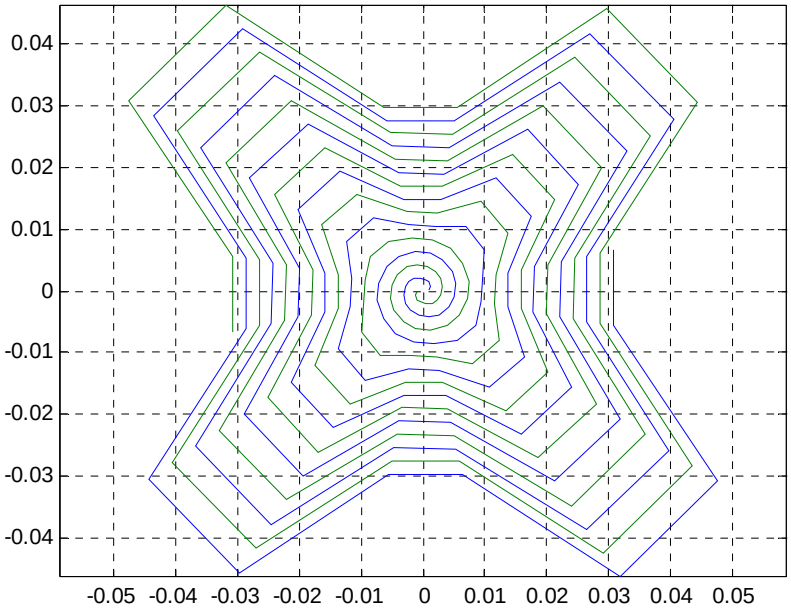

Figure 4.14 Result of second genetic algorithm optimization.

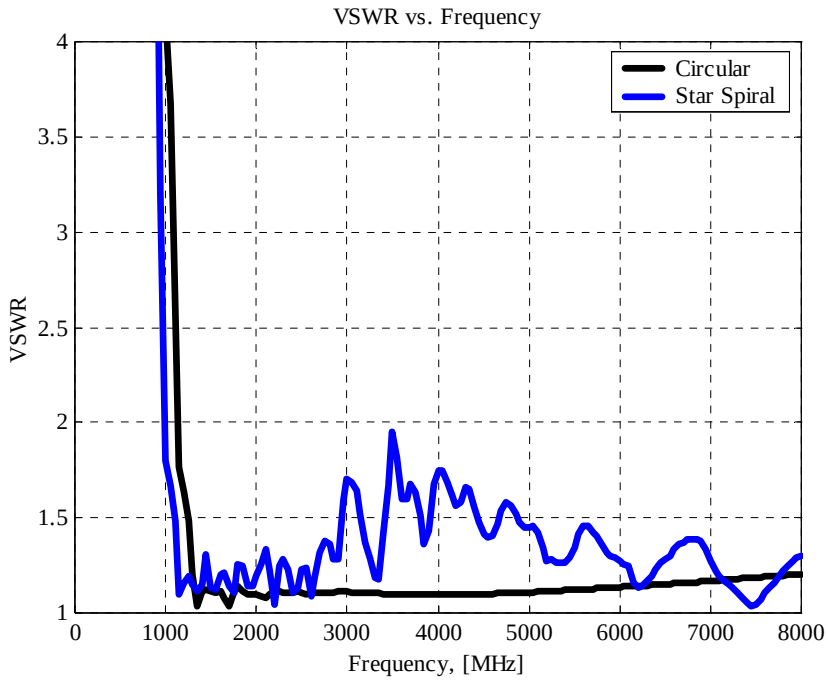

Figure 4.15 VSWR comparison for circular spiral and result of second genetic algorithm optimization (Fig. 4.14).

It is apparent from the previous GA runs that a comprehensive optimization is needed to achieve the desired outcome of increased size reduction and a smooth VSWR curve. The final GA run was setup as follows to optimize all six of the star spiral parameters:

$$\begin{aligned} r_2 &\Rightarrow & r_2 &\le 0.0511 \rightarrow 9\,bits/10^4 \\ N &\Rightarrow & N &\le 16 \rightarrow 4\,bits+1 \\ dr &\Rightarrow & 7\,bits&/10^5 \\ v &\Rightarrow & 6\,bits& \\ taper &\Rightarrow & 9\,bits& \\ trans &\Rightarrow & trans &\le total\ segments \rightarrow 8\,bits \end{aligned} \tag{4.6}$$

The total linear extent of each star spiral in the optimization was restricted to a maximum of 0.1022m so that each chromosome could be compared to an equivalent circular spiral of radius 0.0511m. This restriction made it much easier to evaluate the performance of each chromosome. Also, from experience gained through trial and error of many simulations it is known that certain geometries do not yield effective antennas, and these types of antennas have been monitored and assigned high cost values without using CPU

time to simulate them in NEC4. For example, star spirals where the total linear extent is much larger than twice the outer radius, r_2, have erratic VSWR performance and poor antenna gain. Furthermore, antennas with an effective radius less than 0.047m and spirals with a ratio of maximum radius to outer radius, r_2, less than 1.4 are assigned high cost values and are not simulated to save time. These types of spiral geometries are known to give limited size reduction.

The cost function used to evaluate each chromosome is fairly complex and a bit arbitrary, but is based on trial and error over many GA runs using the problem formulation defined above. Spirals that did not meet the geometry requirements were assigned a cost of 300 and were not simulated. All other spirals were simulated in NEC4 and evaluated based on their VSWR and low frequency cutoff. If the VSWR for a particular chromosome never went below 2:1, then that chromosome was assigned a cost of 99. A spiral that had a VSWR that went below 2:1 at some point but did not stay below 2:1 over the entire frequency band being simulated was assigned a cost of the frequency index plus twice the maximum VSWR of the spiral. The last category is a spiral with a VSWR that goes below 2:1 at some frequency and stays there throughout the whole frequency band of interest. This chromosome was assigned a cost of the frequency index plus the VSWR.

Now, it is necessary to define a few terms. The frequency index is the index of the frequency point just above where the VSWR goes below 2:1. For example, a start frequency of 800MHz and a step frequency of 50MHz were used in this GA. So, if the VSWR went below 2:1 at 875MHz then the frequency index was 3. The maximum VSWR is defined as the VSWR maximum for the frequency band above the frequency index value. It is obvious from the maximum VSWR parameter whether a spiral maintains less than a 2:1 VSWR over the entire frequency band. The geometry restrictions for this GA run are setup to give an optimum antenna with less than a 2:1 VSWR for frequencies between 800-850MHz and greater, which equates to a cost function less than 4.

The results of the final GA optimization are $r_2 = 0.0429m$, $N = 16$ turns, $dr = 0.00009$, $v = 14$, $taper = 413$, and $trans = 174$. The star spiral is plotted in Fig. 4.16 and has a last turn circumference of 0.3644m and an effective radius of 0.0507m.

The VSWR for the star spiral of Fig 4.16 and its equivalent circular spiral is plotted in Fig. 4.17. The low frequency cutoff for the star spiral is 848MHz and 1019MHz for the equivalent circular spiral. The star spiral has an 18.8% increase in last turn circumference and a 16.8% decrease in low frequency cutoff compared to the equivalent circular spiral. The star spiral of Fig. 4.16 has the best size reduction of all of the various star spirals presented in this chapter. It also has a size reduction very close to that expected based on the increase in last turn circumference. The gaps in the star spiral between the circular center and the star shape of the last couple of turns are very interesting and will be investigated further in the next section. The result is unexpected since the GA optimization was setup to provide a smooth transition between the circular center and the outer star shaped spiral.

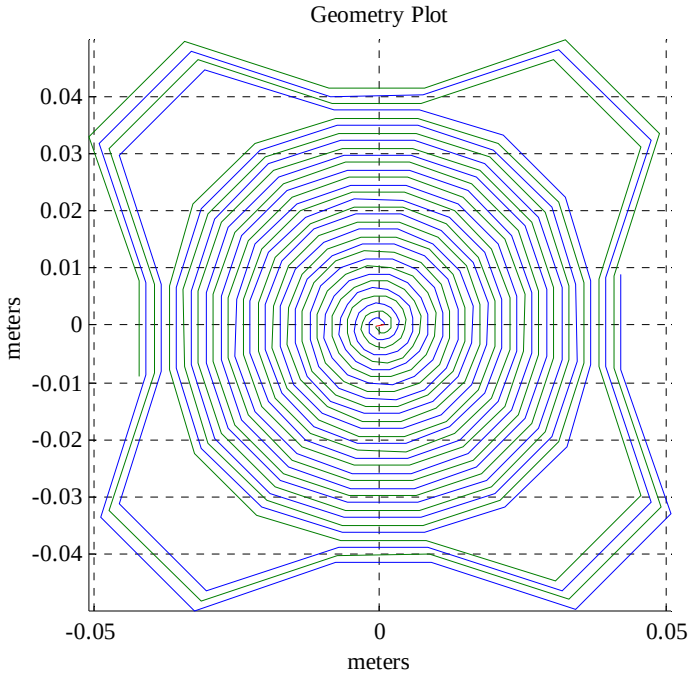

Figure 4.16 Result of final genetic algorithm optimization.

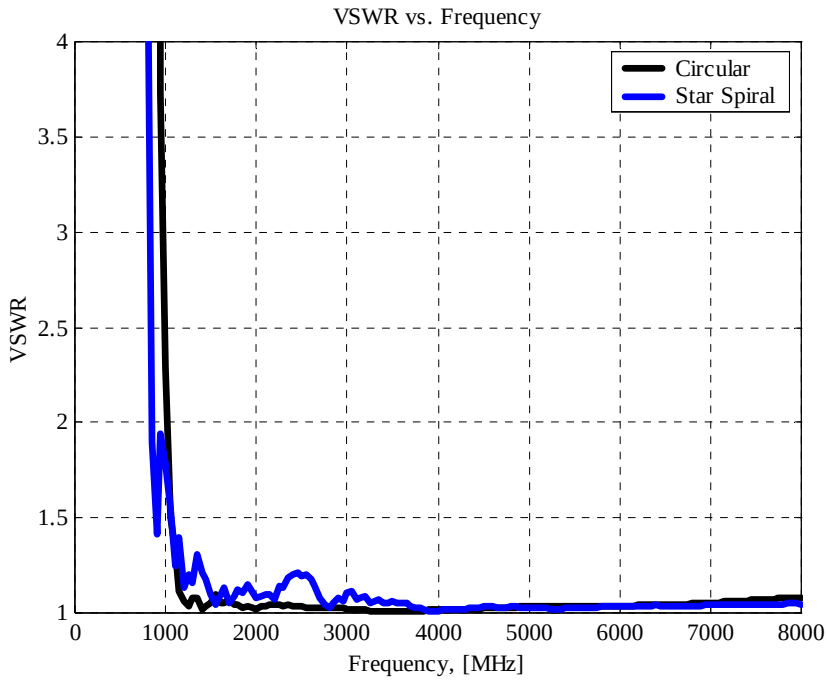

Figure 4.17 VSWR comparison for circular spiral and result of final genetic algorithm optimization.

4.3 Analysis of Optimized Star Spiral Antenna

The goal used in the early genetic algorithm runs was to create a smooth transition between the circular center and the outer star shape. The final optimized star spiral of Fig. 4.16 showed that the approach does not necessarily produce the best spiral in terms of size reduction. However, creating a smoother transition between the circular center and the outer star shape can reduce the VSWR spike around 950MHz that is seen in Fig. 4.17. The smoother transition can be achieved by reducing the parameter, *taper* . It was found that using $taper = 260$ gives the best performance. The final version of the star spiral that will be used in this thesis is presented in Fig. 4.18 and a comparison of the VSWR curves for the two star spirals is shown in Fig. 4.19. The VSWR spike around 950MHz has been greatly reduced and the VSWR is quite smooth over the entire frequency range of interest while maintaining an 849MHz low frequency cutoff.

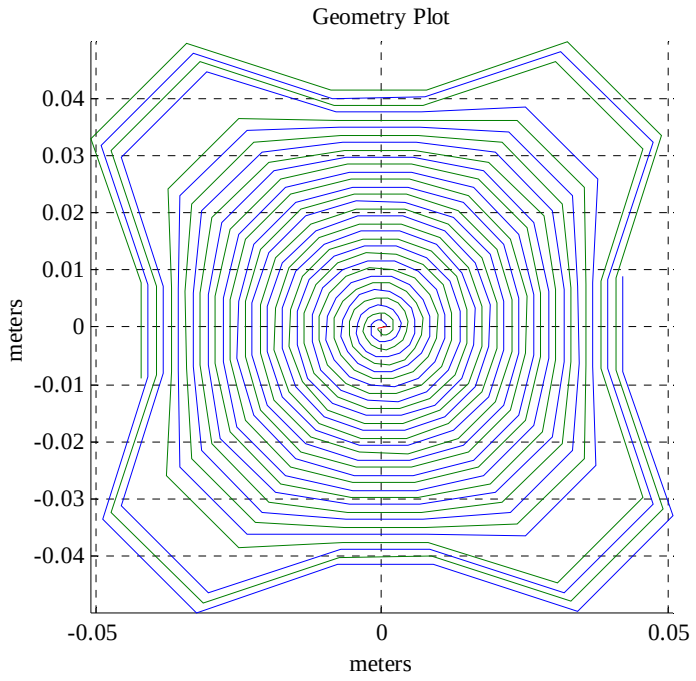

Figure 4.18 Star spiral with *taper* = 260 .

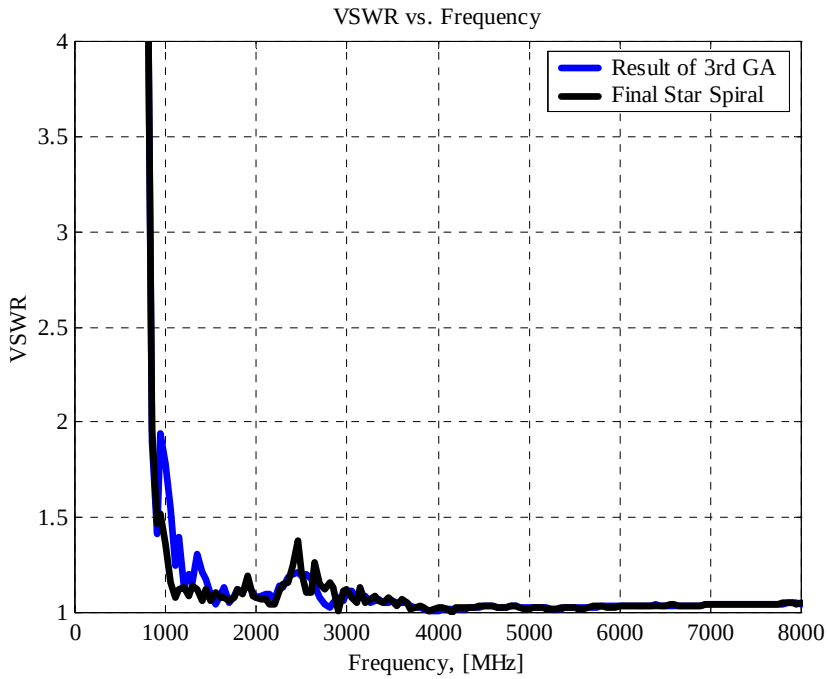

Figure 4.19 VSWR comparison for result of final genetic algorithm optimization (Fig. 4.18) and final star spiral to be used throughout this thesis.

The operation of the star spiral can be better understood by examining the current along the spiral for the star spiral of Fig. 4.16 with $taper = 413$, the star spiral of Fig. 4.18 with $taper = 260$, the star spiral of Fig. 4.20 with $taper = 227$, and an equivalent circular spiral. The star spiral in Fig. 4.20 was designed to have a smooth transition between the circular center and the outer star shape. The VSWR for the four spirals is shown in Fig. 4.21. The star spiral with $taper = 260$ is clearly the best combination of low frequency cutoff and a stable VSWR across the frequency band. The reason that the star spiral with $taper = 260$ has the best VSWR performance can be seen be examining the current along the spirals. The genetic algorithm cost function was designed to give the largest reduction in low frequency cutoff for a given increase in the outer circumference of the spiral. This was accomplished by minimizing the reflections of the current from the end of the spiral. This effect can be seen by examining the current plots of Fig. 4.22 for various frequencies. The oscillations in the plots are a result of the reflection of the current from the end of the spiral arm. As expected for Fig. 4.22 (a)-(c), where the frequency is low, the circular spiral has a large amount of current reflection from the end of the spiral. These plots also predict the results of the VSWR plot of Fig 4.21. For example, at 900MHz, the star spiral with $taper = 227$ shows the greatest amount of current reflection and also has the highest VSWR compared to the other two star spirals. Also, at 1000MHz and 1100MHz the star spiral with $taper = 413$ has the largest VSWR compared to the other star spirals and it also has the largest current reflection from the end of the spiral. Fig. 4.22(d) shows that for higher frequencies the current reflections for all for of the spirals has been greatly reduced. The same effect was seen in Chapter 2 where conductivity loss and resistive loading was used to reduce the reflections from the end of the spiral, which also reduced the low frequency cutoff of the spiral.

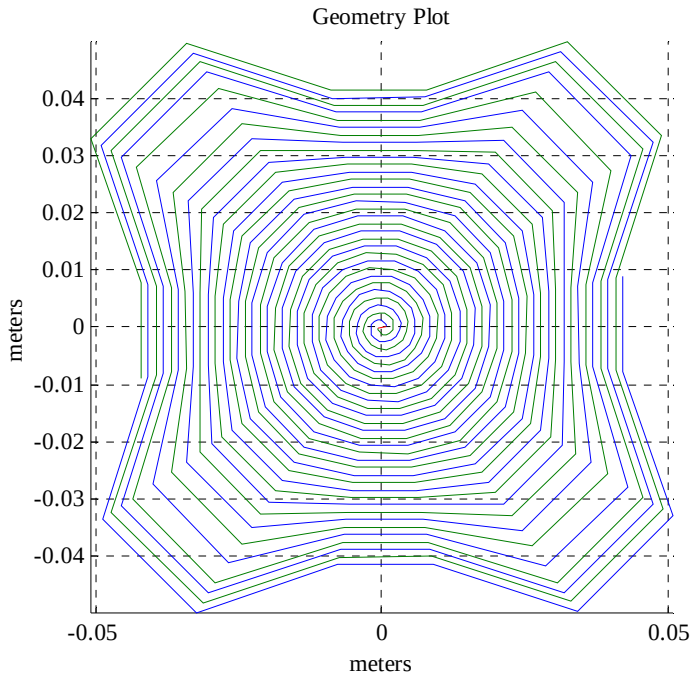

Figure 4.20 Star spiral with *taper* = 227 .

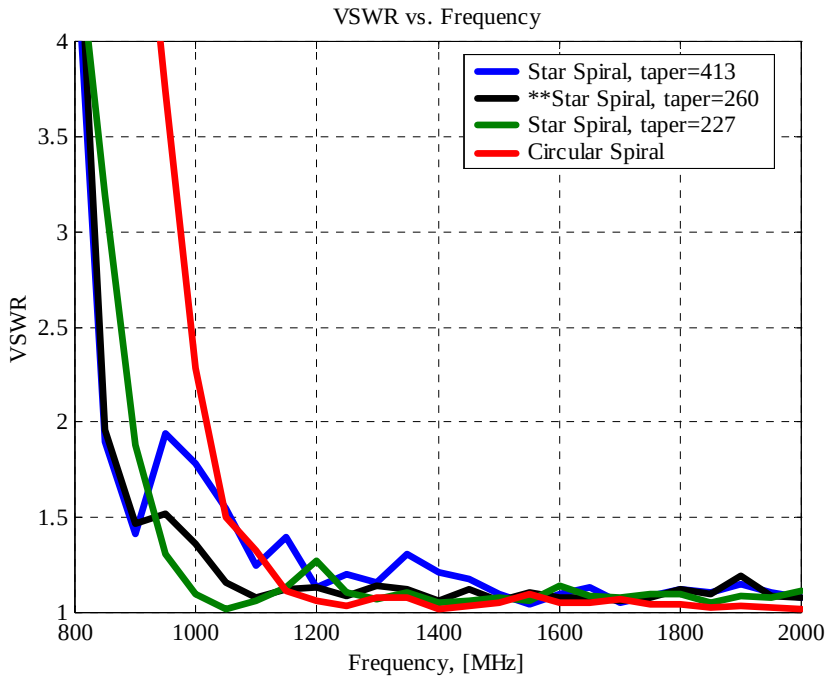

Figure 4.21 VSWR comparison of three different star spirals with the circular spiral.

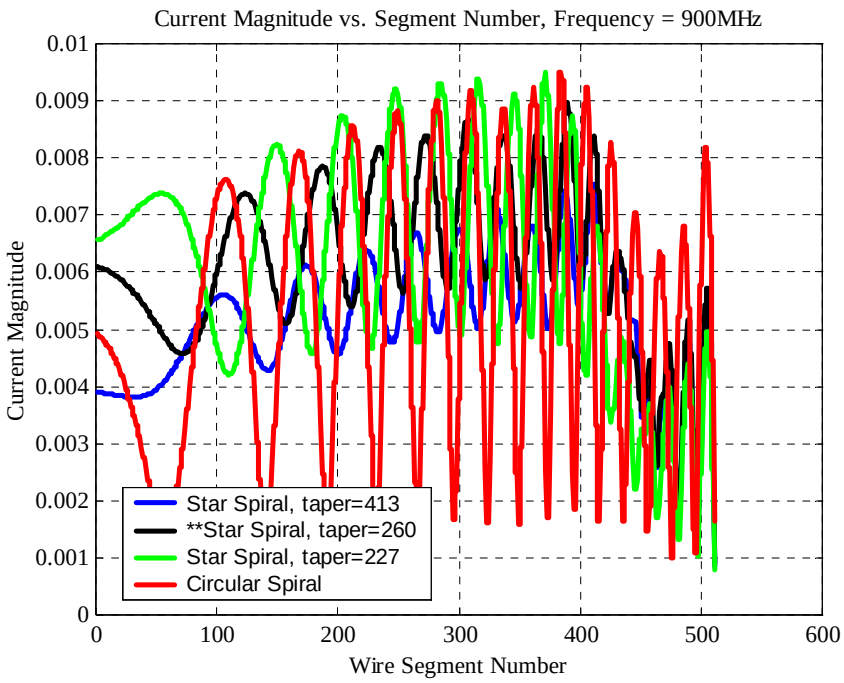

(a) Frequency = 900MHz

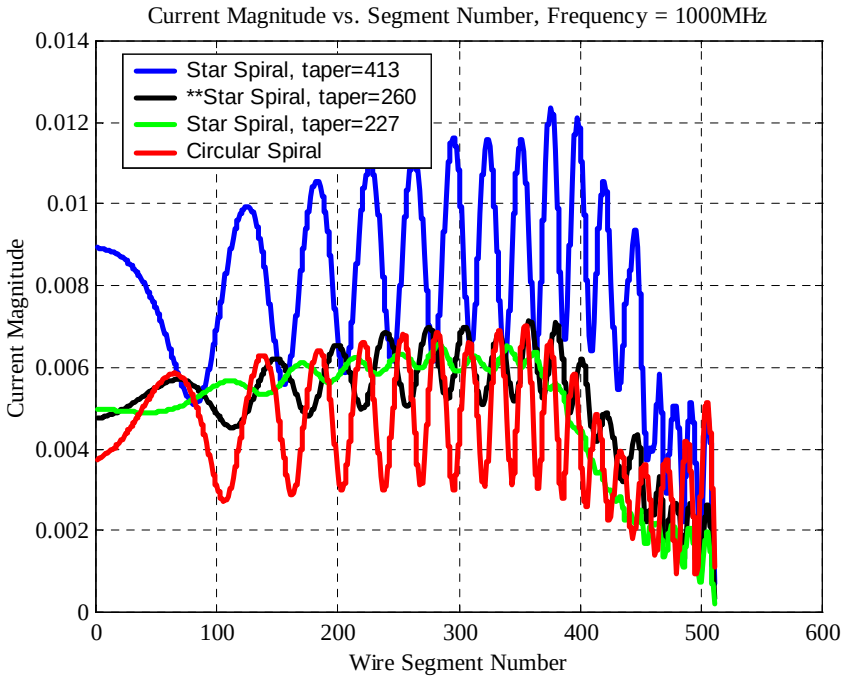

(b) Frequency = 1000MHz

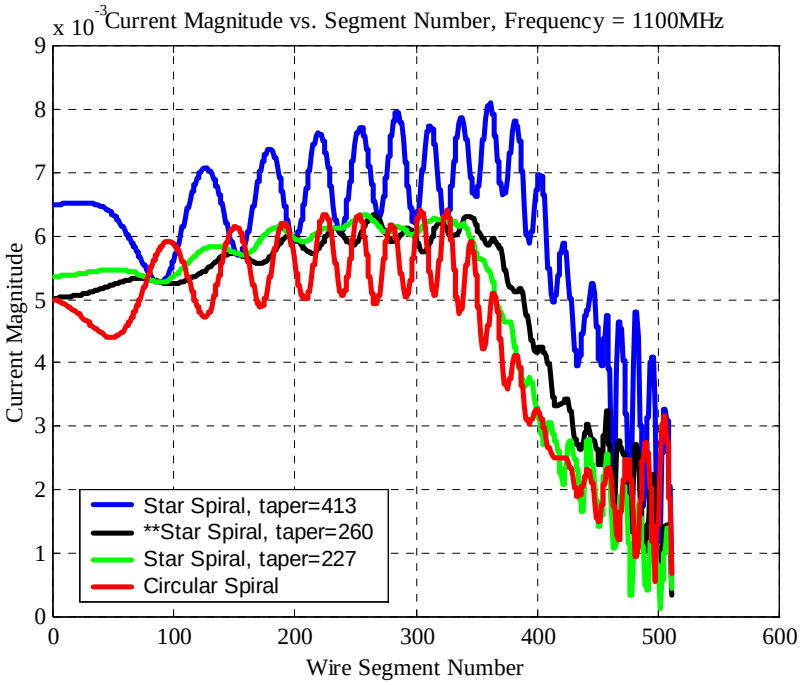

(c) Frequency = 1100MHz

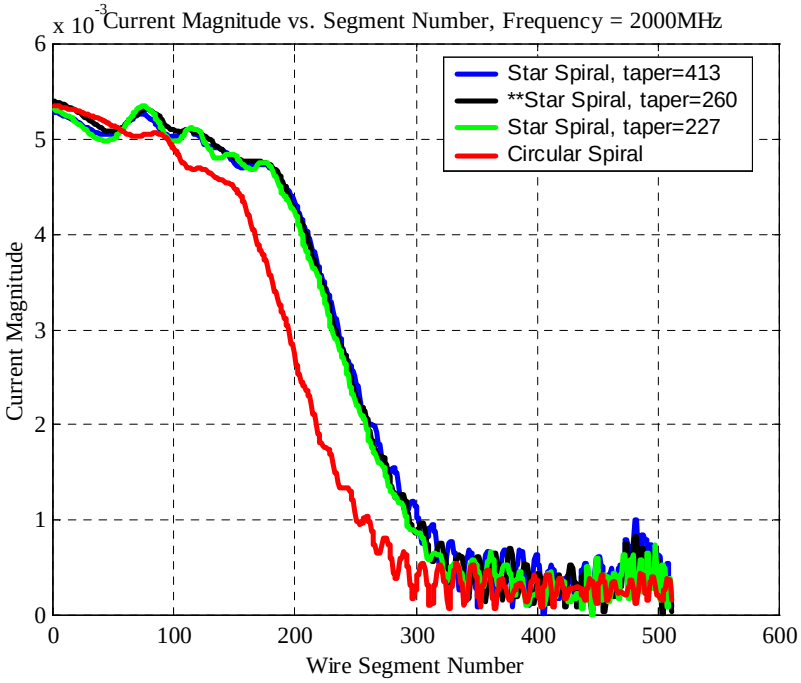

(d) Frequency = 2000MHz

Figure 4.22 Current magnitude comparison of three different star spirals with the circular spiral at various frequencies.

The star spiral can be further evaluated by comparing it to the square spiral. The square spiral is a common slow-wave spiral and provides a good basis for comparison. The square spiral, shown in Fig. 4.23, is equivalent to the star spiral in terms of its linear extent, and both the star spiral and square spiral are compared to the circular Archimedean spiral. The VSWR for each of the three spirals is plotted in Fig. 4.24 and the relevant parameters are summarized in Table 4.3. The square spiral has a greater size reduction than the star spiral but the star spiral is significantly more efficient in terms of γ, its actual size reduction compared to its expected size reduction, as seen in the last column of Table 4.1. Also, the star spiral has a slightly better VSWR than the square spiral does across the frequency band. Furthermore, the square spiral does not allow for improved array packing like the star spiral. A comparison of the boresight gain and axial ratio of the star spiral with a square spiral and a circular Archimedean spiral are plotted in Fig. 4.25 and Fig. 4.26, respectively. The gain of the star spiral is approximately 2dB better than the square spiral, and it also matches the gain of the circular spiral quite well. Furthermore, the star spiral out performs the square spiral in terms of boresight axial ratio, particularly at higher frequencies. For applications where circular polarization (axial ratio less than 3dB) is necessary a 4-arm star spiral can be used to greatly improve the axial ratio. Also, the circular center of the star spiral allows the performance of the star spiral to converge towards that of the circular spiral at higher frequencies while still providing size reduction.

Table 4.3 Comparison of performance improvement in star spiral versus the square spiral.

Spiral	f_L, [MHz]	Circumference, [m]	% Improvement in Frequency	% Improvement in Circumference	γ = % Frequency / % Cicumference
Circular	1018	0.3068	N/A	N/A	N/A
Square	822	0.3931	19.3	28.1	0.69
Star	849	0.3644	16.6	18.8	0.88

Table 4.4 Geometry parameters for spirals discussed in Chapter 4.

Spiral	r_2 , [m]	N	dr , [m]	v	*taper*	*trans*	seg/turn
Circular, Fig. 4.1	0.05	16	0	NA	NA	NA	40
Zig-zag, Fig. 4.2	0.05	16	7×10^{-6}	NA	NA	NA	40
Pointed Star, Fig. 4.3	0.05	16	1.35×10^{-4}	NA	NA	NA	16
Star, Fig. 4.7	0.038	16	8.9×10^{-5}	0	NA	NA	16
Star, Fig. 4.8	0.038	16	1.43×10^{-4}	24	NA	NA	16
Star, Fig. 4.12	0.03149	7	3.1×10^{-4}	7	110	NA	16
Star, Fig. 4.14	0.03149	7	3×10^{-4}	8	113	5	16
Star, Fig. 4.16	0.0429	16	9×10^{-5}	14	413	174	16
Star, Fig. 4.18	0.0429	16	9×10^{-5}	14	260	174	16
Star, Fig. 4.20	0.0429	16	9×10^{-5}	14	227	174	16

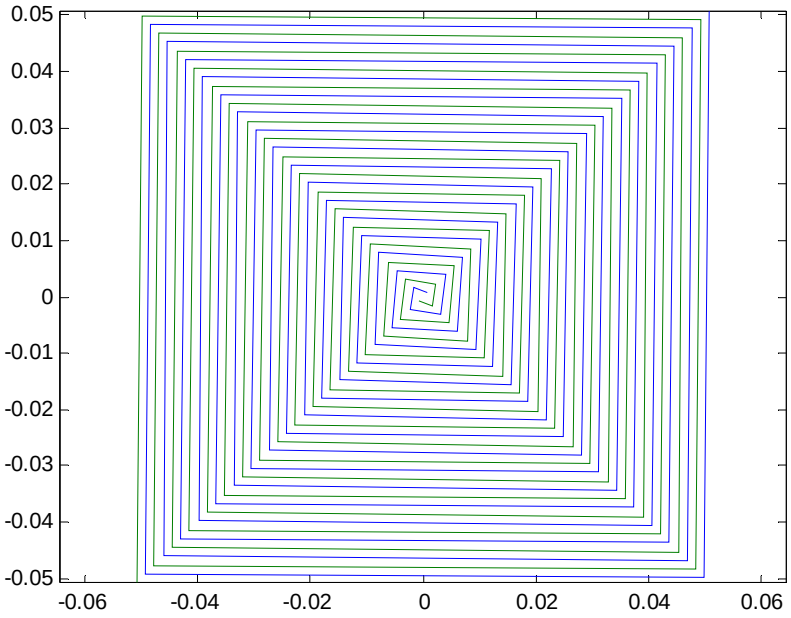

Figure 4.23 Square spiral for comparison to star spiral.

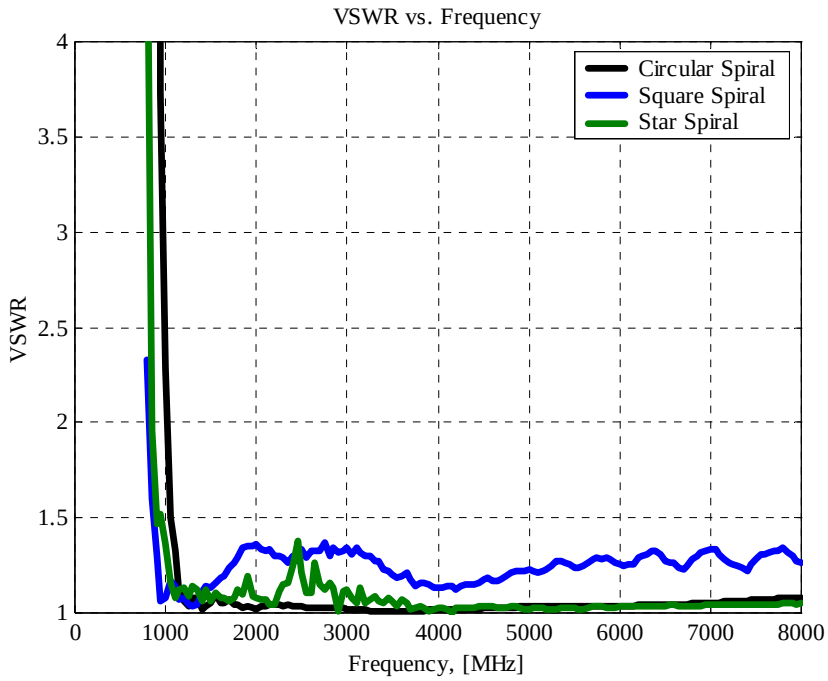

Figure 4.24 VSWR comparison of star spiral with a square and circular spiral.

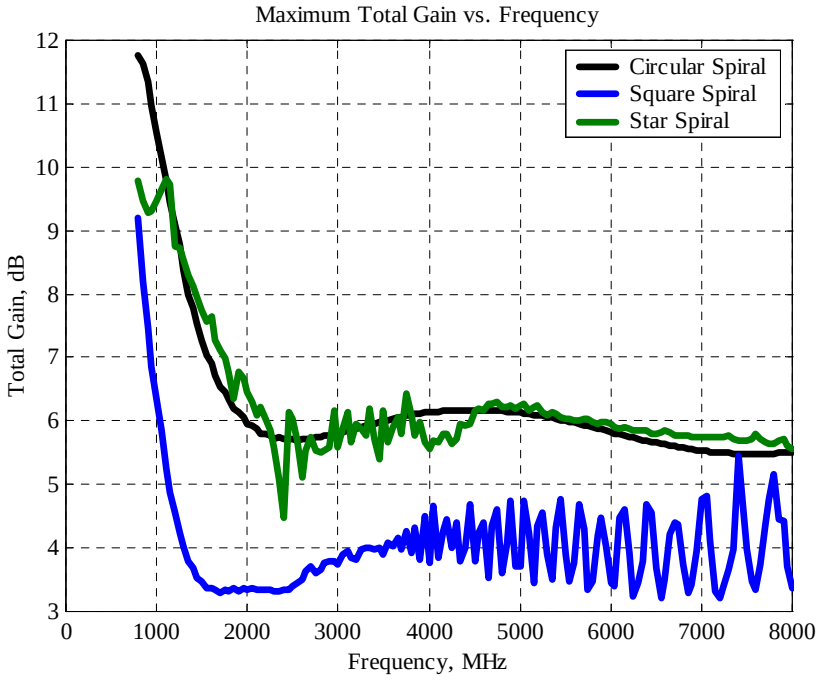

Figure 4.25 Boresight gain comparison of star spiral with a square and circular spiral.

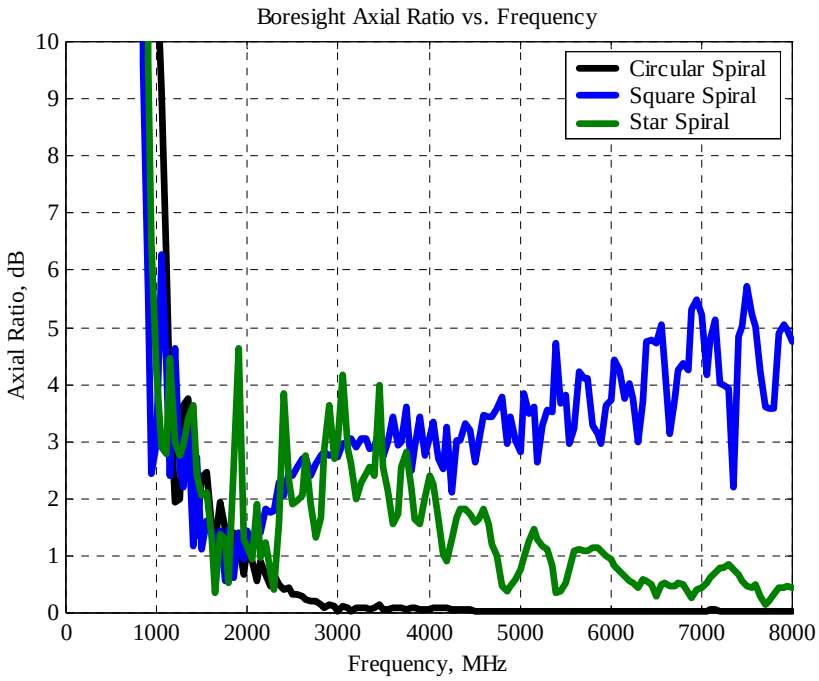

Figure 4.26 Axial ratio comparison of star spiral with a square and circular spiral.

4.4 Measurements of Star Spiral

Impedance, gain, pattern, and axial ratio measurements were performed on the star spiral. The measurements are needed to verify the operation of the star spiral and for validation of the NEC4 simulations. The measurements will be compared to the measurements of the circular Archimedean spiral presented in Chapter 2. A picture of the measured star spiral with parameters $r_2 = 0.0429m$, $N = 16$ turns, $dr = 0.00009$, $v = 14$, $taper = 260$, and $trans = 174$ is shown in Fig. 4.27. This star spiral is equivalent in linear extent to the circular spiral measured in Chapter 2. Refer to Table 4.4 for comparison to other spiral geometries.

The measured input impedance of the star spiral is plotted in Fig. 4.28. The star spiral was fed using a coaxial "Y-shaped" feed as seen in Fig. 5.14(b). The measured star spiral compares favorably with the measured circular spiral and it also matches the trends seen in the simulated data. Both the measured star and circular spiral input impedances decrease with increasing frequency instead of remaining constant as expected. This may

be due to the losses in the structure as frequency increases. Fig. 4.29 shows the VSWR for the star spiral and the circular spiral. Both spirals are referenced to 150Ω and the simulated data is matched to 188Ω as always. The measured low frequency cutoff (VSWR < 2:1) of the circular spiral is 946 MHz and 774 MHz for the star spiral to give an 18.2% size reduction, which is slightly more than the 16.6% predicted in simulations. Also, the effect of the small loss in the spiral is apparent from the reduction in low frequency cutoff from 849 MHz to 774 MHz for the measured star spiral compared to the simulated value. An equivalent square spiral was also measured to have a low frequency cutoff of 781 MHz for a size reduction of 17.5%, which is less than the star spiral's 18.2%. The square spiral results are also shown in Fig. 4.29.

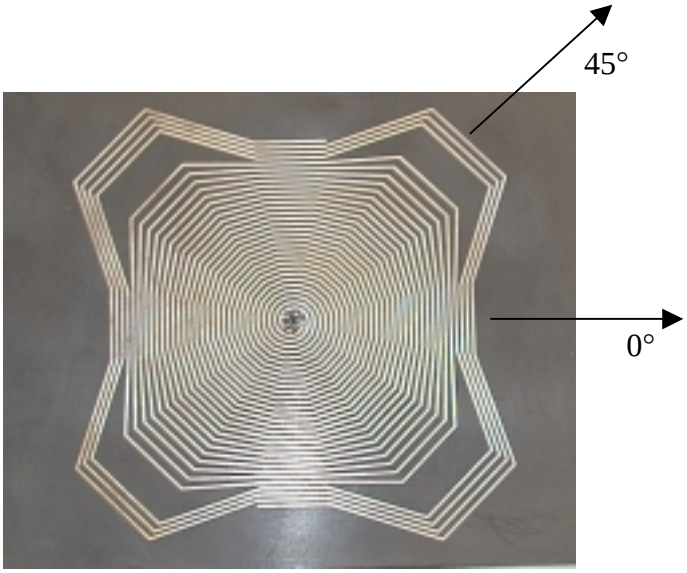

Figure 4.27 Measured star spiral antenna.

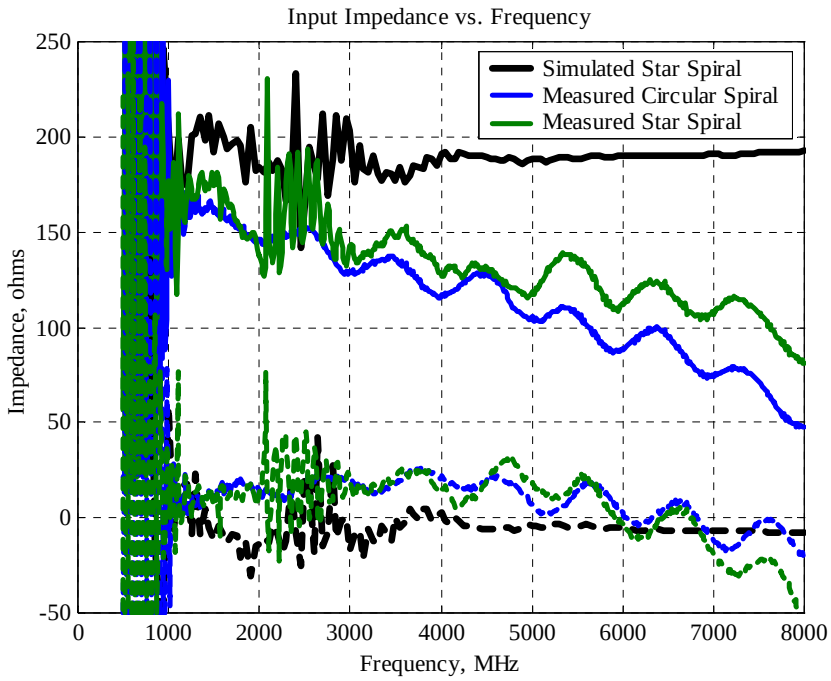

Figure 4.28 Comparison of the measured input impedance of the star spiral of Fig. 4.27 with the circular spiral of Fig. 2.30 and simulated data.

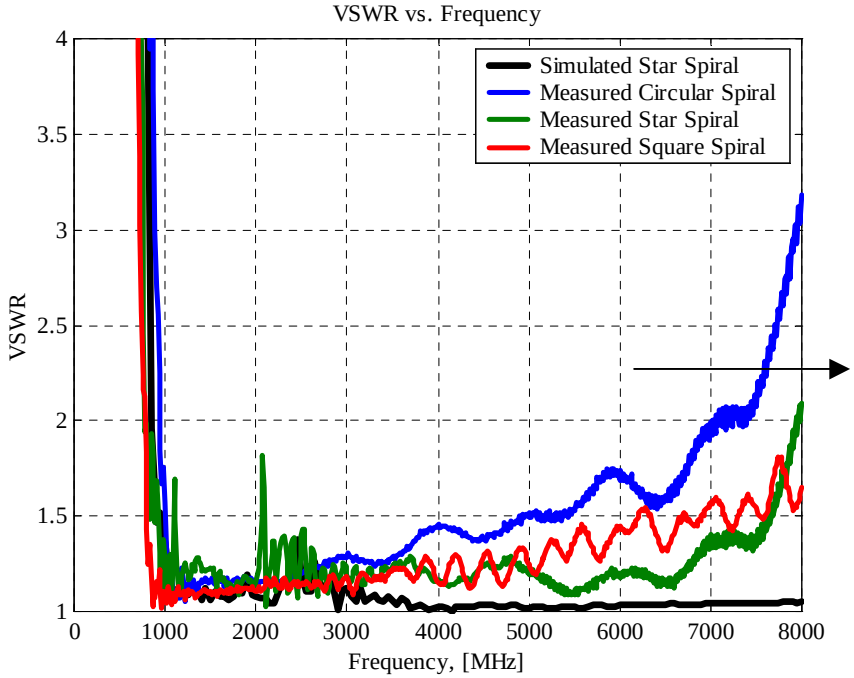

Figure 4.29 Comparison of the measured VSWR of star spiral of Fig. 4.27 with circular spiral of Fig. 2.30, square spiral of Fig. 4.23, and simulated data. The measured data is referenced to 150Ω.

The measured gain of the star spiral is presented in Fig. 4.30. The star spiral gain is shown for both $0°$ and $45°$ as defined in Fig. 4.27. In theory the boresight gain should be the same in both planes but the measurements show some variation. As in Chapter 2 for the circular spiral, the gain is also plotted with the impedance mismatch, $1-|\Gamma|^2$, and hybrid loss removed, which is shown in Fig. 4.31. The measured gain of the star spiral matches very well with that of the circular spiral. It also matches well with the simulated gain at higher frequencies. Both the circular and star spirals showed a higher simulated gain at lower frequencies than was measured.

Fig. 4.32 shows the measured axial ratio of the star spiral. The simulated and measured axial ratio of the star spiral match pretty well over the frequency band. As expected, the axial ratio of the circular spiral is a little better than that of the star spiral, but the axial ratio of the star spiral is better than 3 dB for most frequencies.

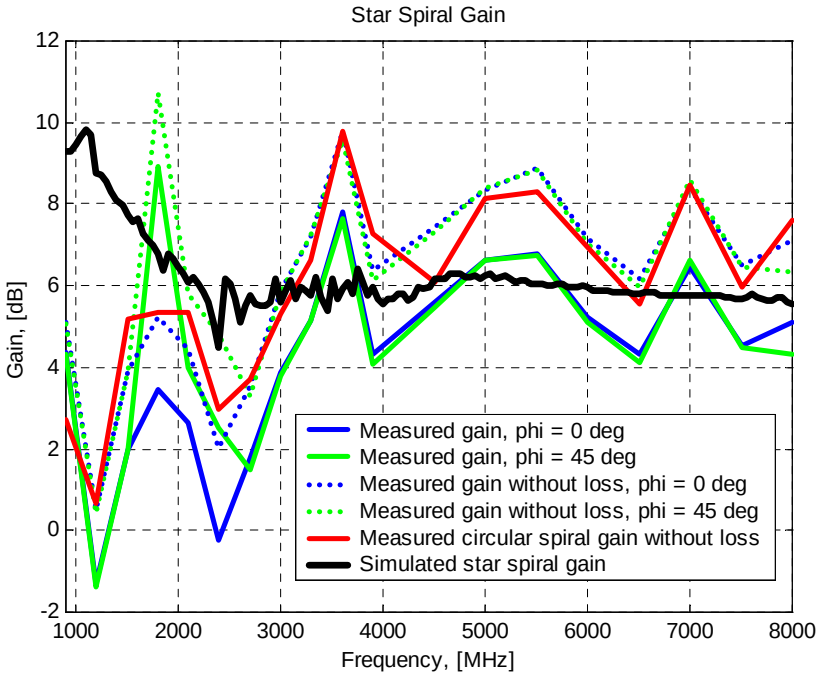

Figure 4.30 Comparison of the measured gain of the star spiral antenna with the circular spiral and simulated data.

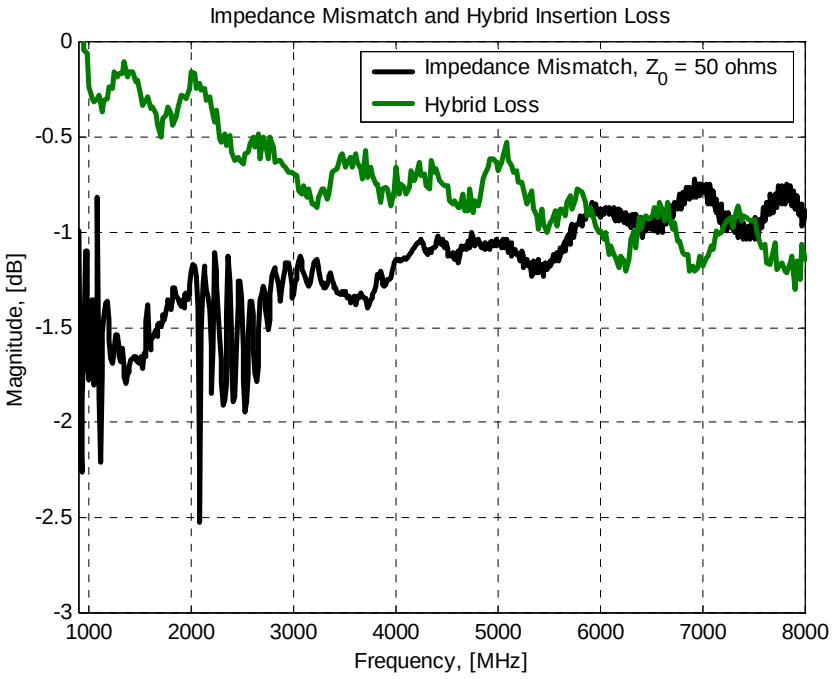

Figure 4.31 Measured impedance mismatch and hybrid loss.

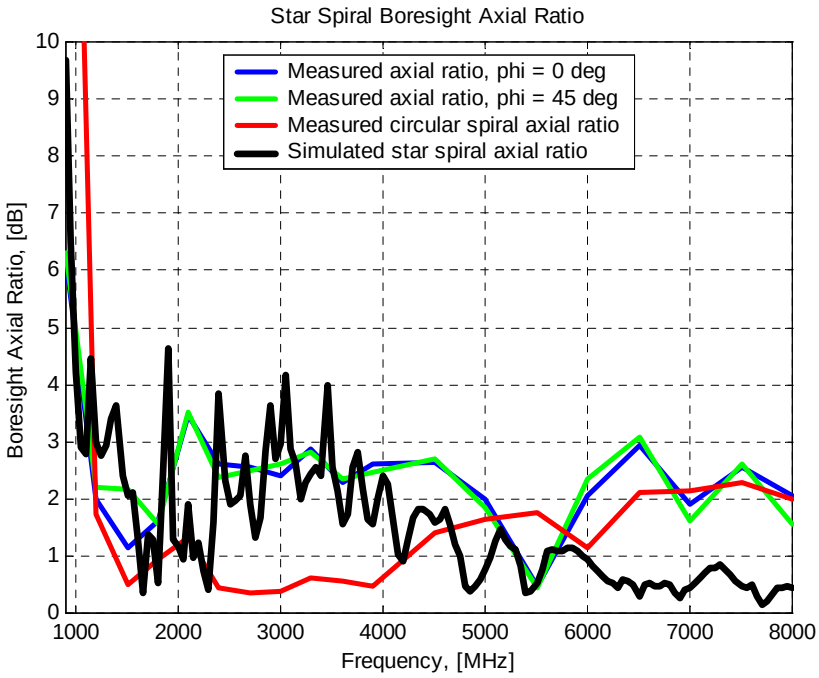

Figure 4.32 Comparison of the measured axial ratio of the star spiral antenna with the circular spiral and simulated data.

The radiation patterns and axial ratio patterns for the star spiral are plotted in Fig. 4.33 and Fig. 4.34, respectively. In general, both patterns match well with simulated results and they are also very similar to the patterns of the circular Archimedean spiral presented in Chapter 2. The radiation patterns and the axial ratio patterns are quite similar in both the $\phi = 0°$ and the $\phi = 45°$ planes as desired, but there is a bit more variation in both patterns for frequencies below 4 GHz. The co-polarized patterns are left circularly polarized and the cross-polarized patterns have right hand circular polarization.

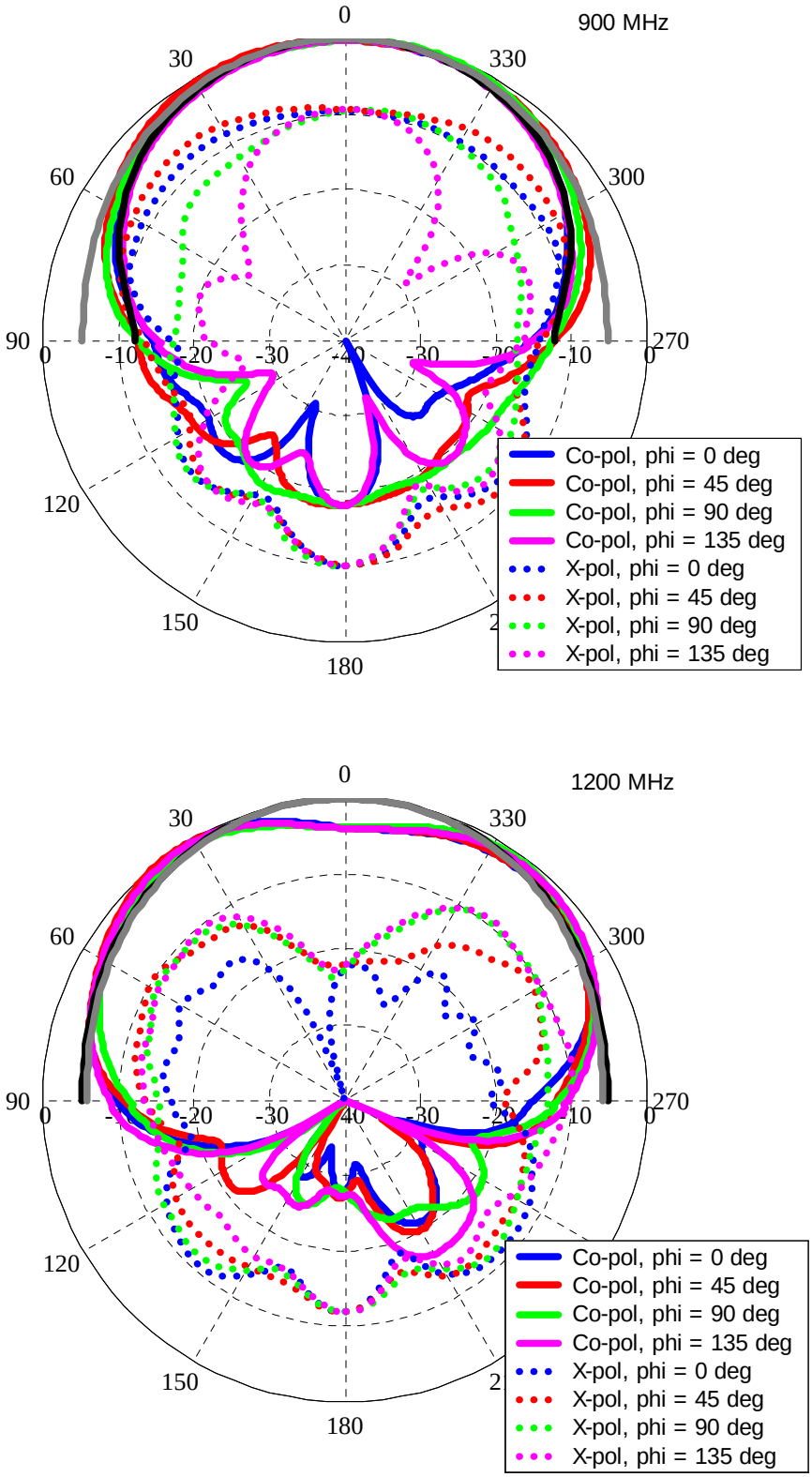

Figure 4.33 Measured star spiral radiation patterns of Fig. 4.27. Theta cuts. Black line is the simulated result for and the gray line is the simulated result for $\phi = 45°$.

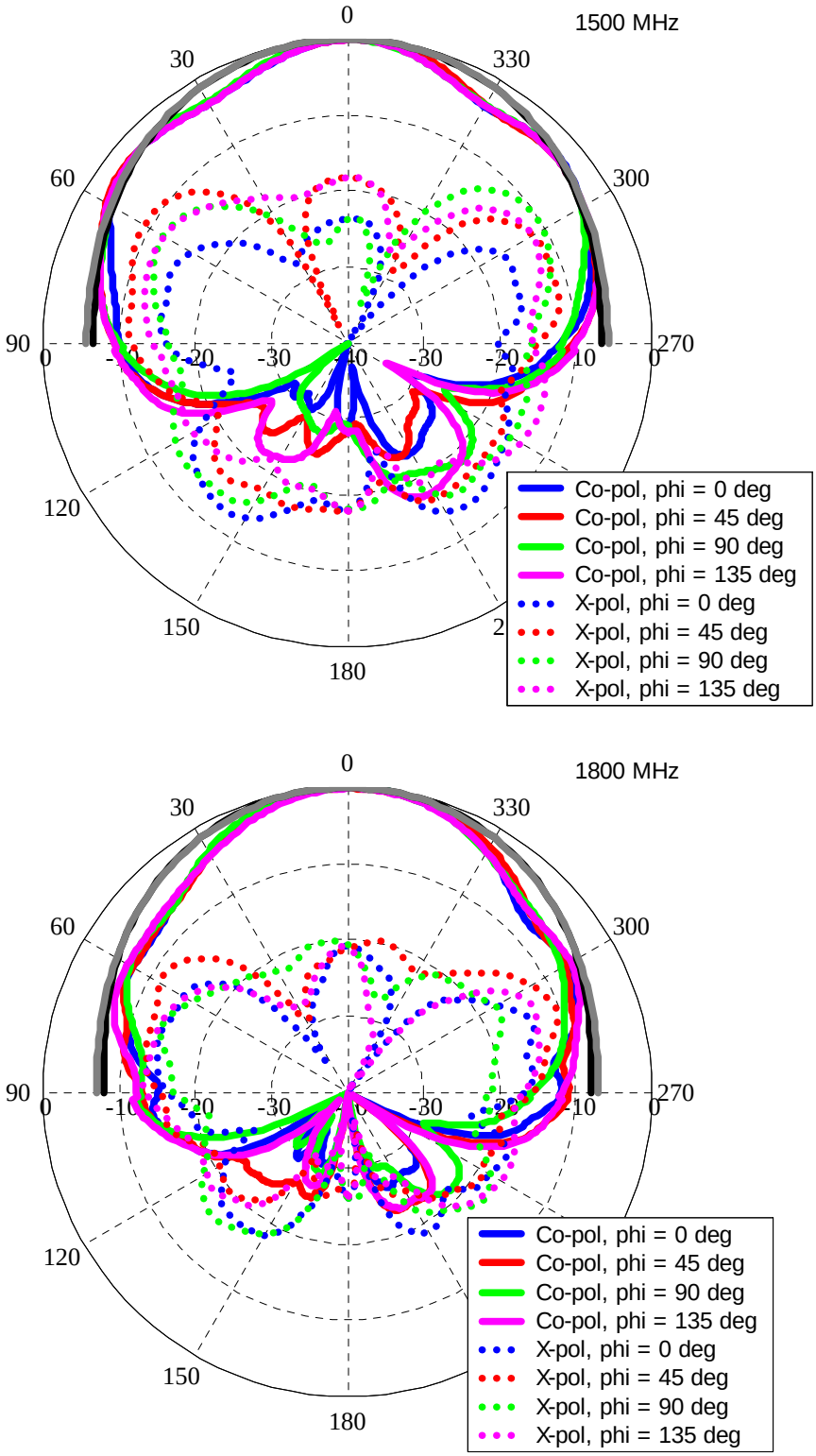

Figure 4.33 (cont) Measured star spiral radiation patterns of Fig. 4.27. Theta cuts. Black line is the simulated result for $\phi = 0°$ and the gray line is the simulated result for $\phi = 45°$.

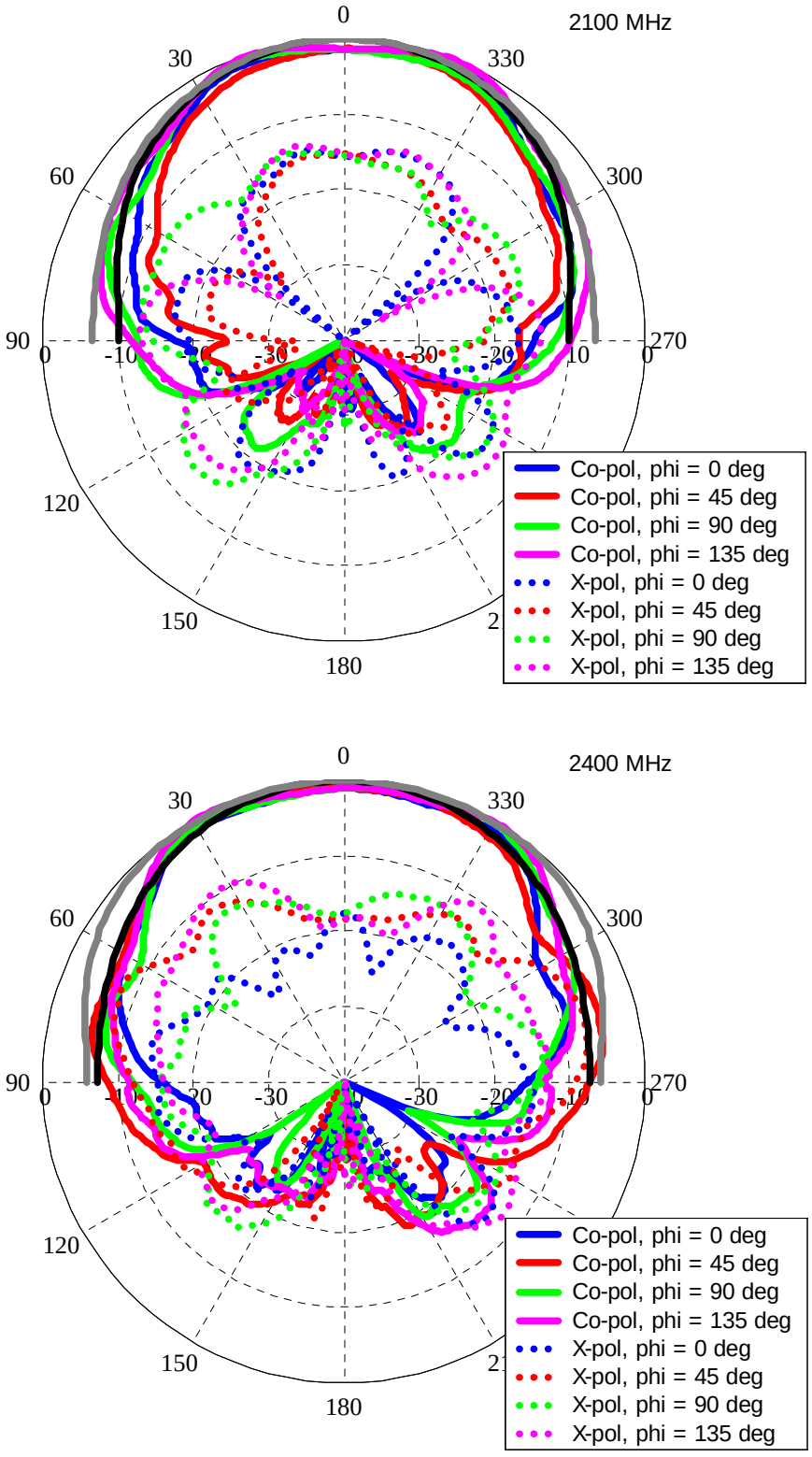

Figure 4.33 (cont) Measured star spiral radiation patterns of Fig. 4.27. Theta cuts. Black line is the simulated result for $\phi = 0°$ and the gray line is the simulated result for $\phi = 45°$.

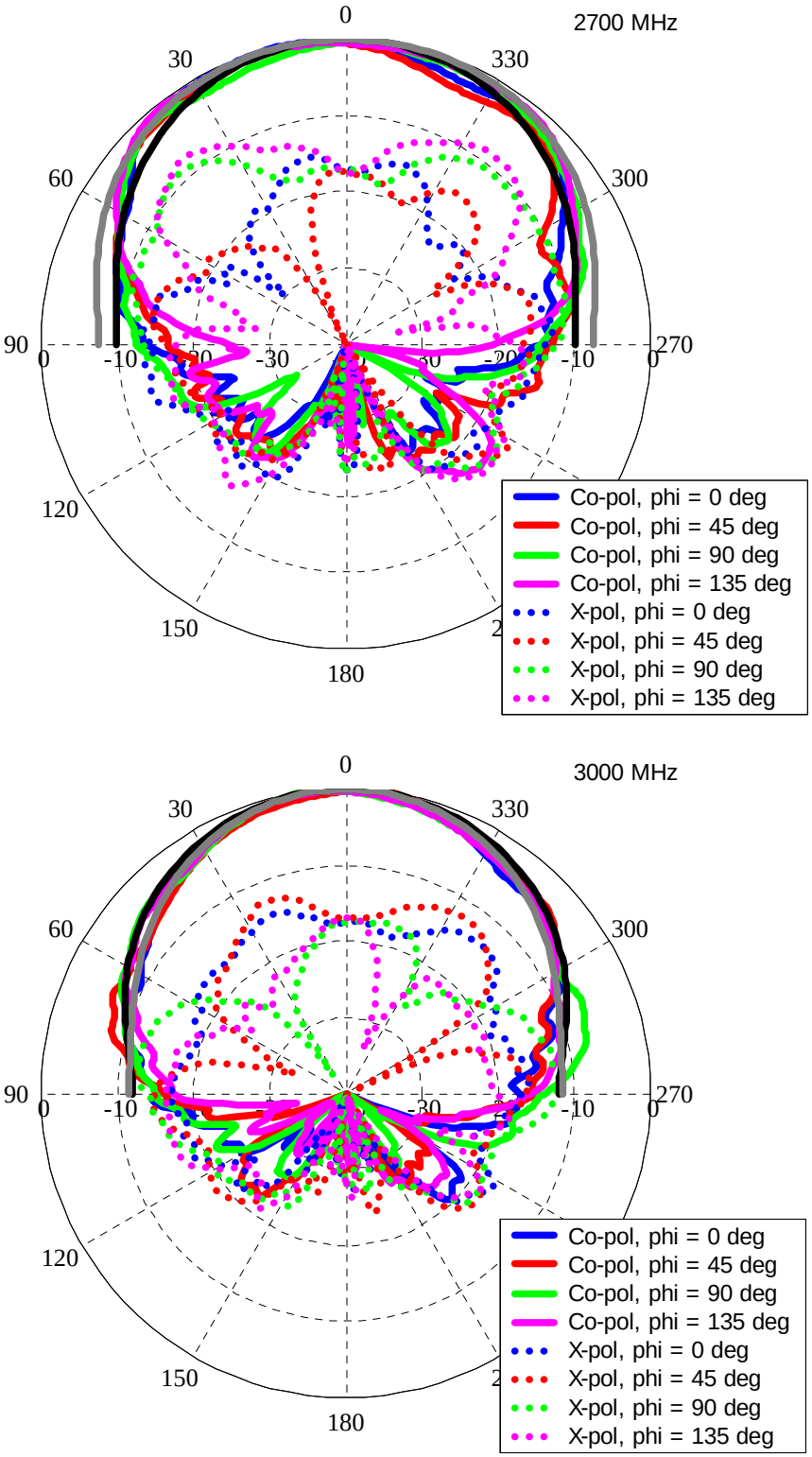

Figure 4.33 (cont) Measured star spiral radiation patterns of Fig. 4.27. Theta cuts. Black line is the simulated result for $\phi = 0°$ and the gray line is the simulated result for $\phi = 45°$.

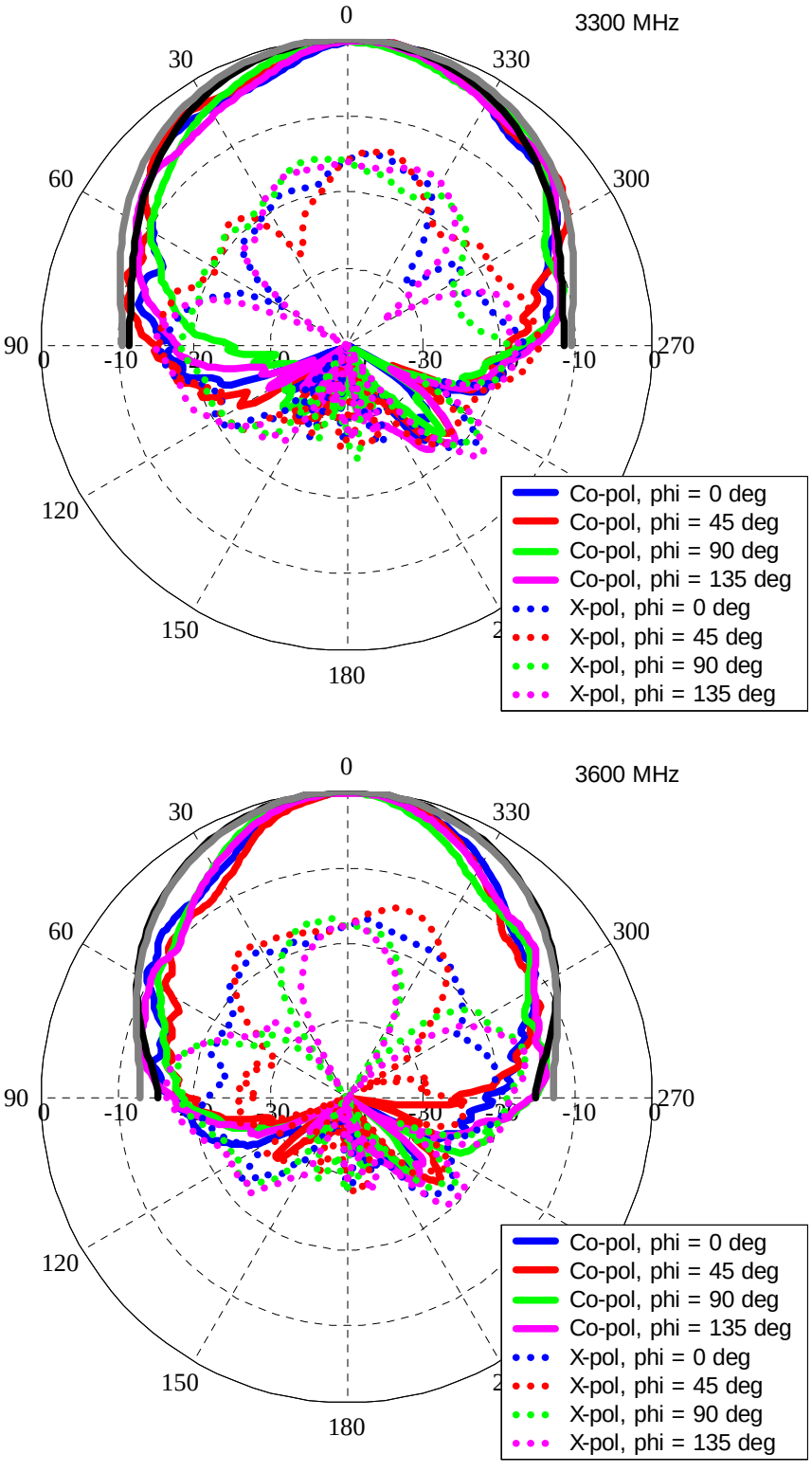

Figure 4.33 (cont) Measured star spiral radiation patterns of Fig. 4.27. Theta cuts. Black line is the simulated result for $\phi = 0°$ and the gray line is the simulated result for $\phi = 45°$.

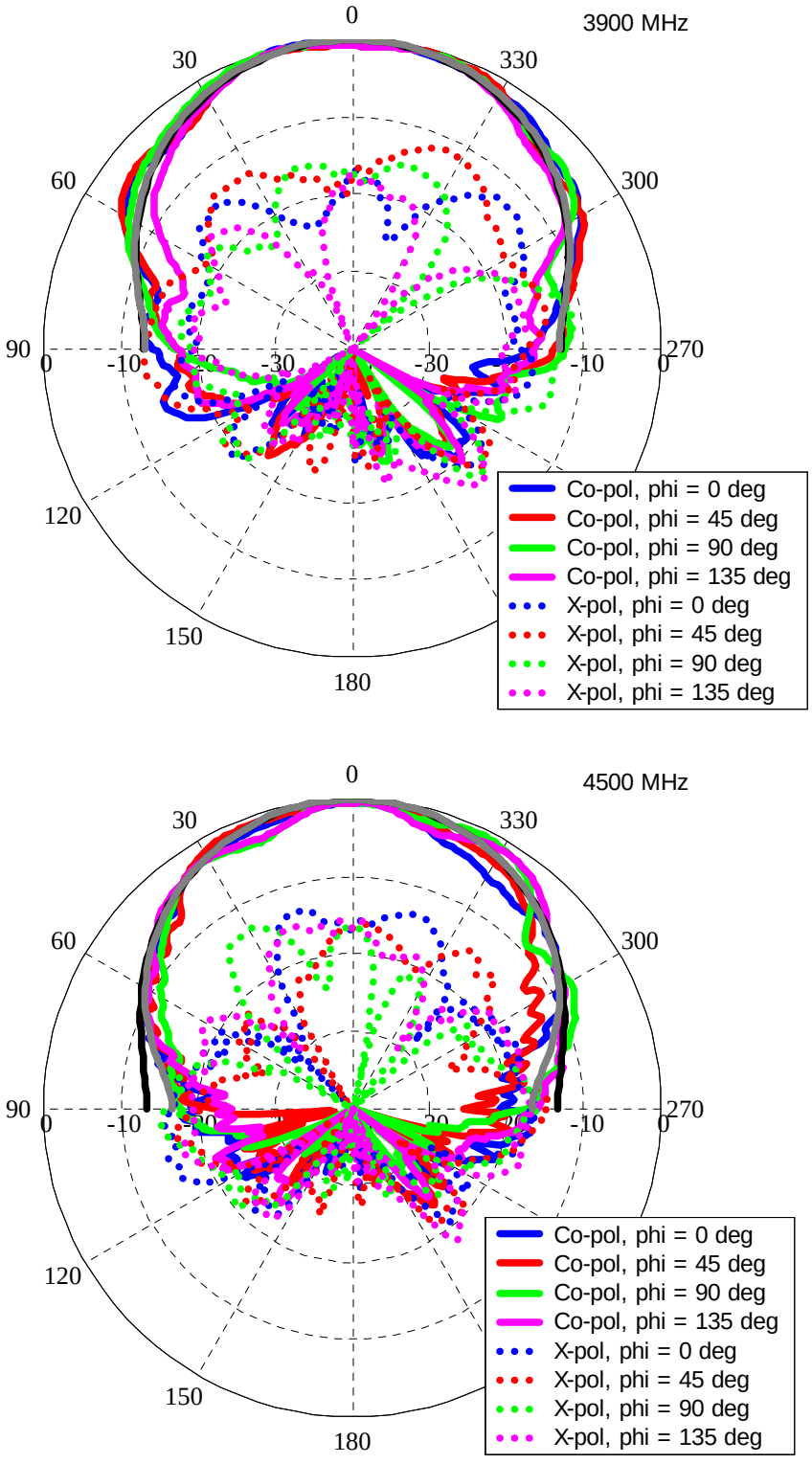

Figure 4.33 (cont) Measured star spiral radiation patterns of Fig. 4.27. Theta cuts. Black line is the simulated result for $\phi = 0°$ and the gray line is the simulated result for $\phi = 45°$.

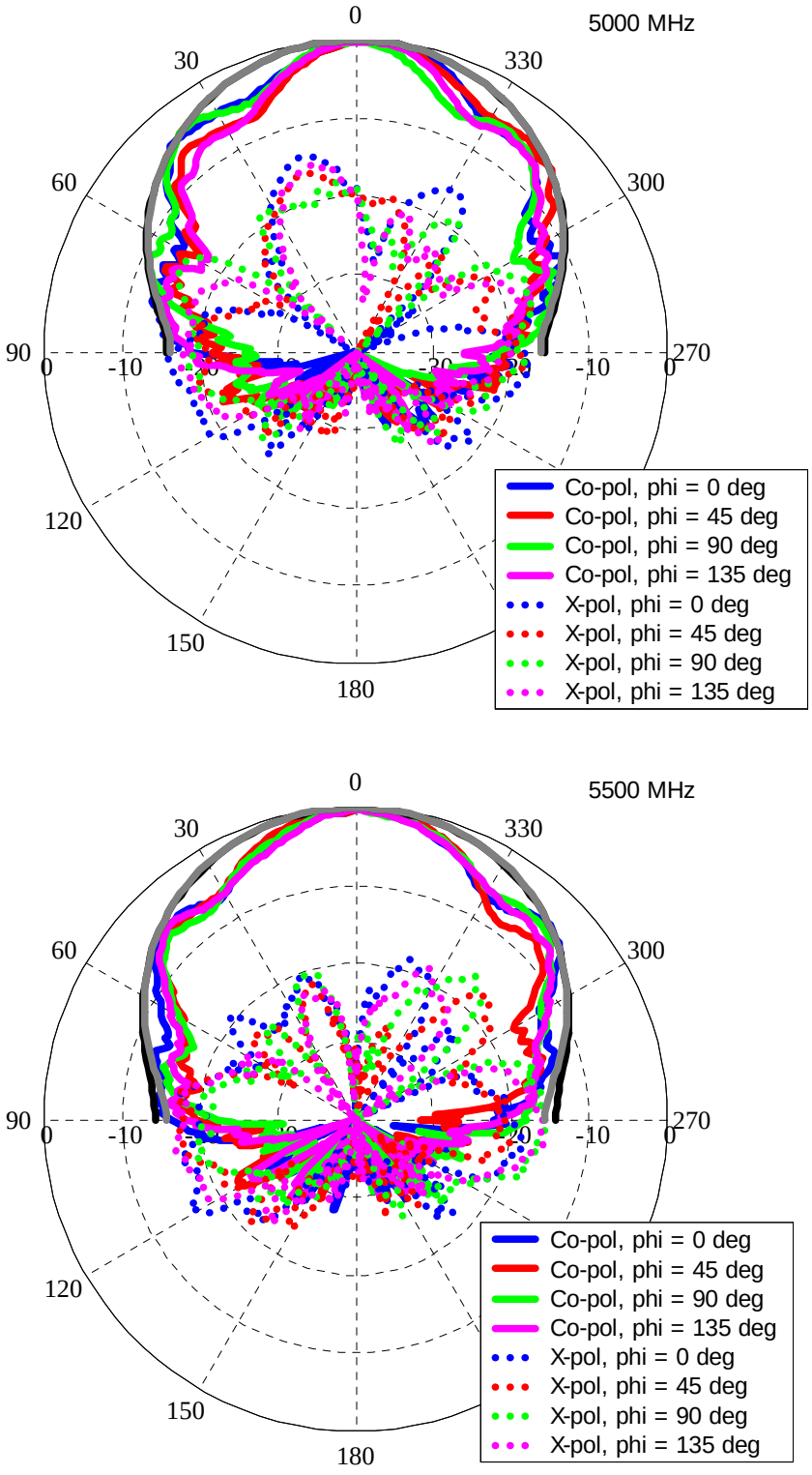

Figure 4.33 (cont) Measured star spiral radiation patterns of Fig. 4.27. Theta cuts. Black line is the simulated result for $\phi = 0°$ and the gray line is the simulated result for $\phi = 45°$.

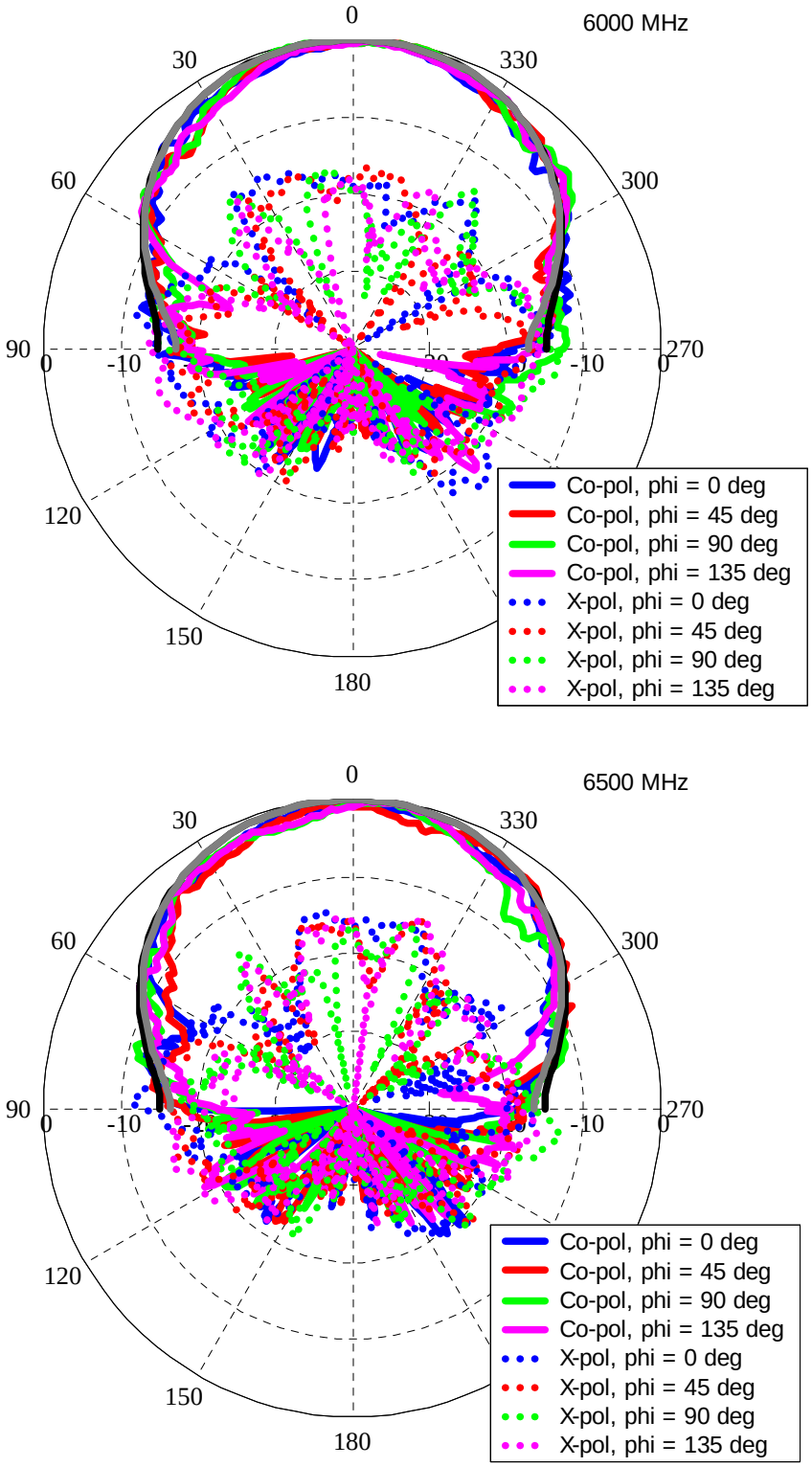

Figure 4.33 (cont) Measured star spiral radiation patterns of Fig. 4.27. Theta cuts. Black line is the simulated result for $\phi = 0°$ and the gray line is the simulated result for $\phi = 45°$.

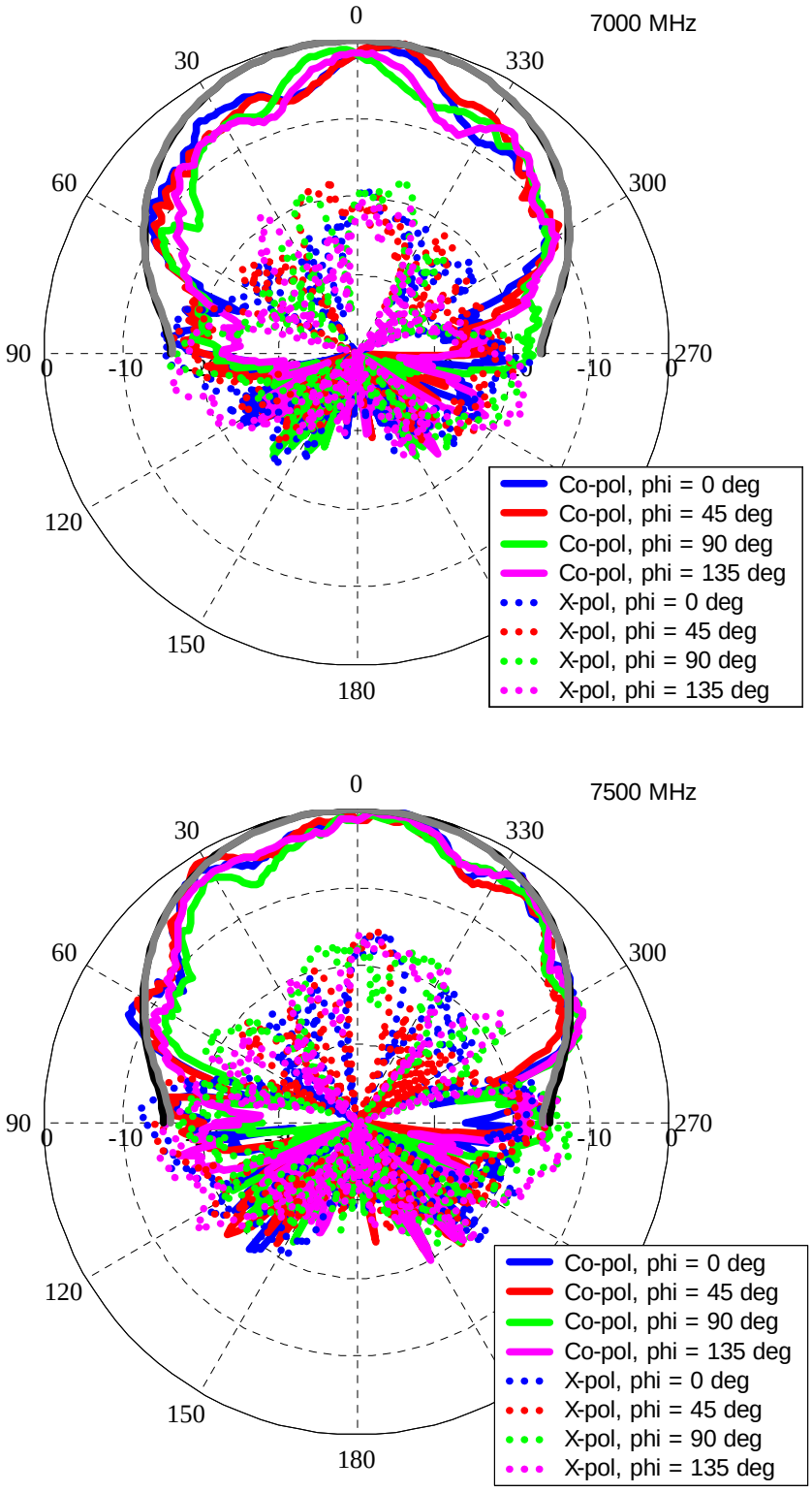

Figure 4.33 (cont) Measured star spiral radiation patterns of Fig. 4.27. Theta cuts. Black line is the simulated result for $\phi = 0°$ and the gray line is the simulated result for $\phi = 45°$.

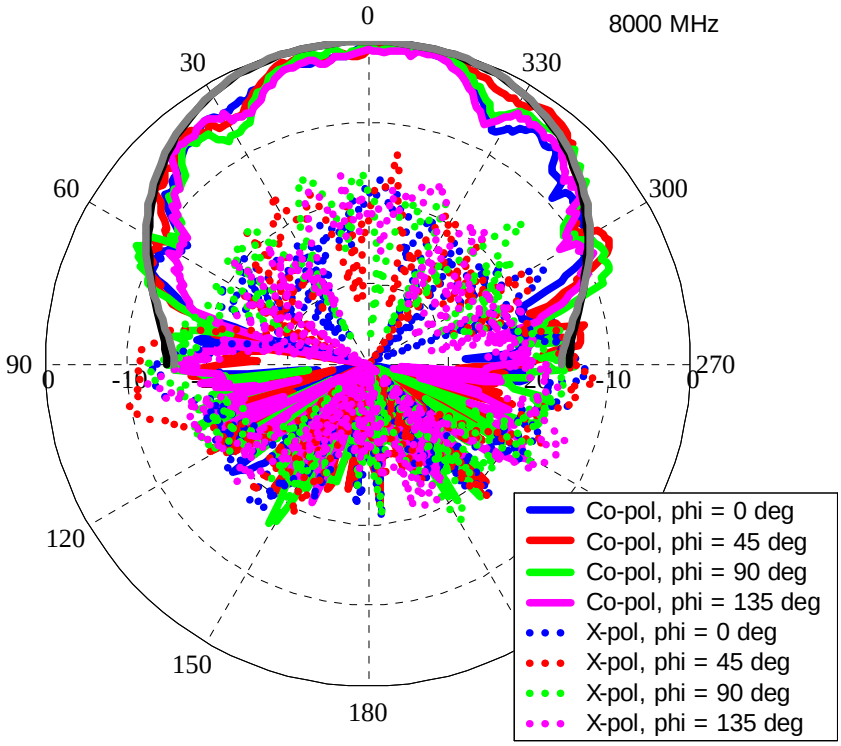

Figure 4.33 (cont) Measured star spiral radiation patterns of Fig. 4.27. Theta cuts. Black line is the simulated result for $\phi = 0°$ and the gray line is the simulated result for $\phi = 45°$.

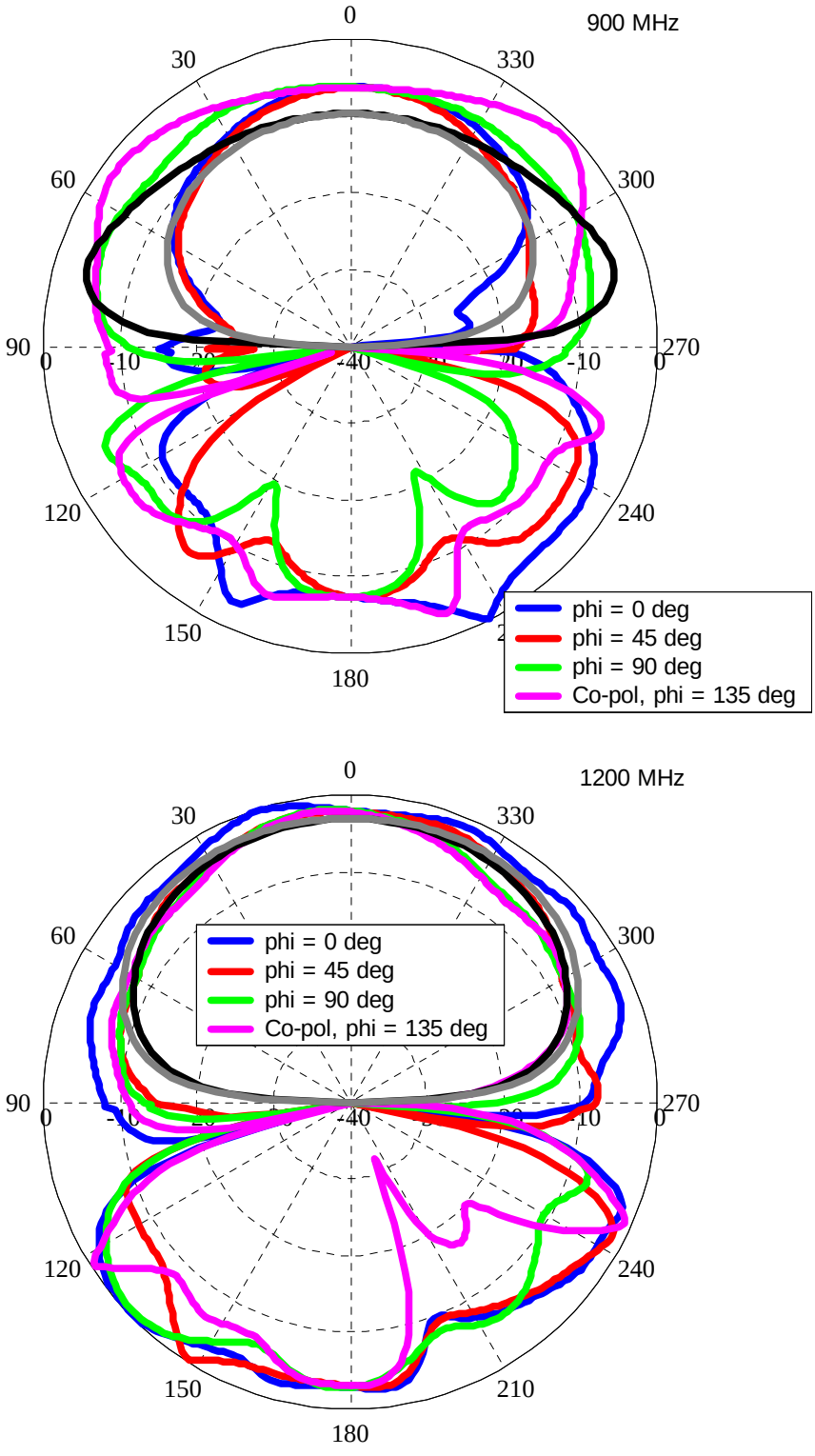

Figure 4.34 Measured star spiral axial ratio patterns of Fig. 4.27. Theta cuts. Black line is the simulated result for $\phi = 0°$ and the gray line is the simulated result for $\phi = 45°$.

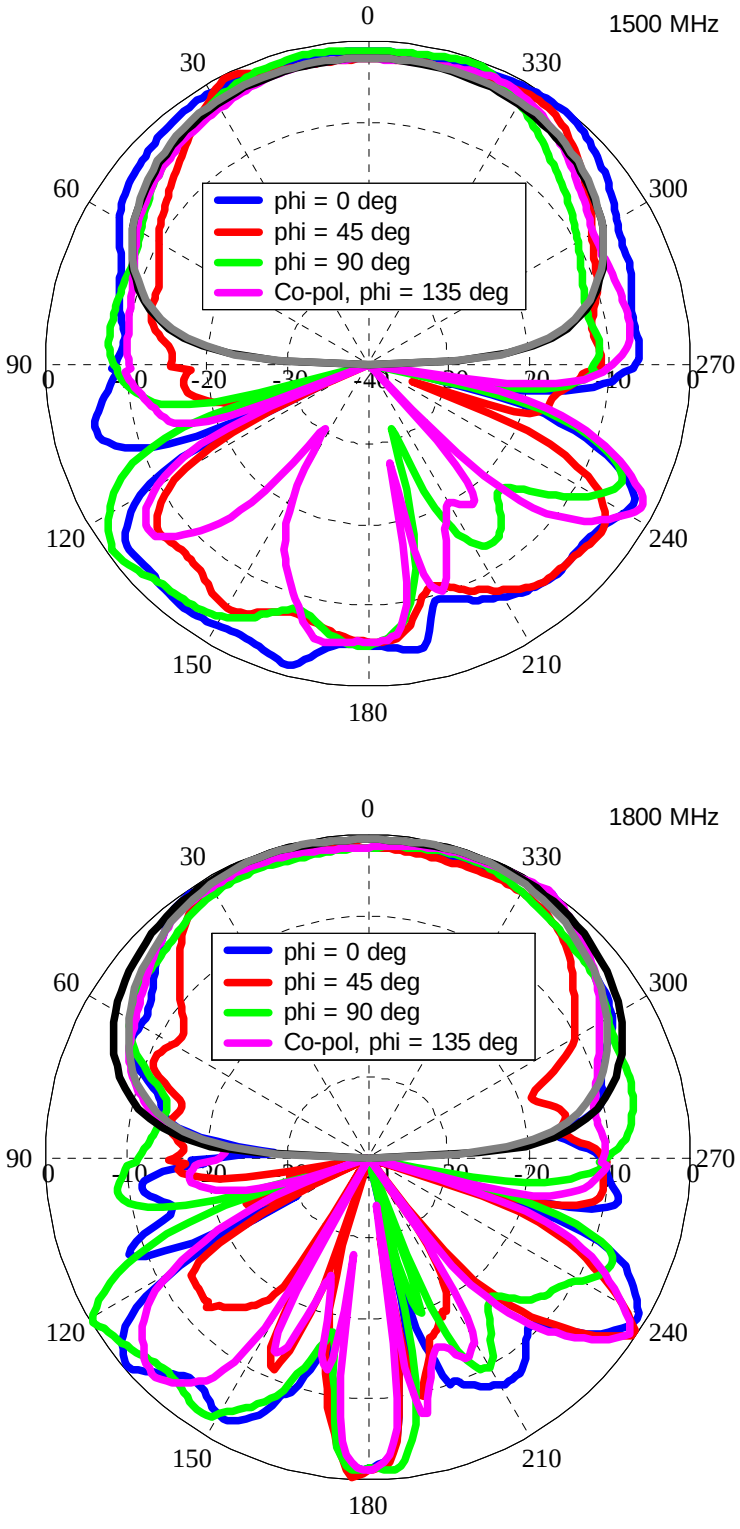

Figure 4.34 (cont) Measured star spiral axial ratio patterns of Fig. 4.27. Theta cuts. Black line is the simulated result for $\phi = 0°$ and the gray line is the simulated result for $\phi = 45°$.

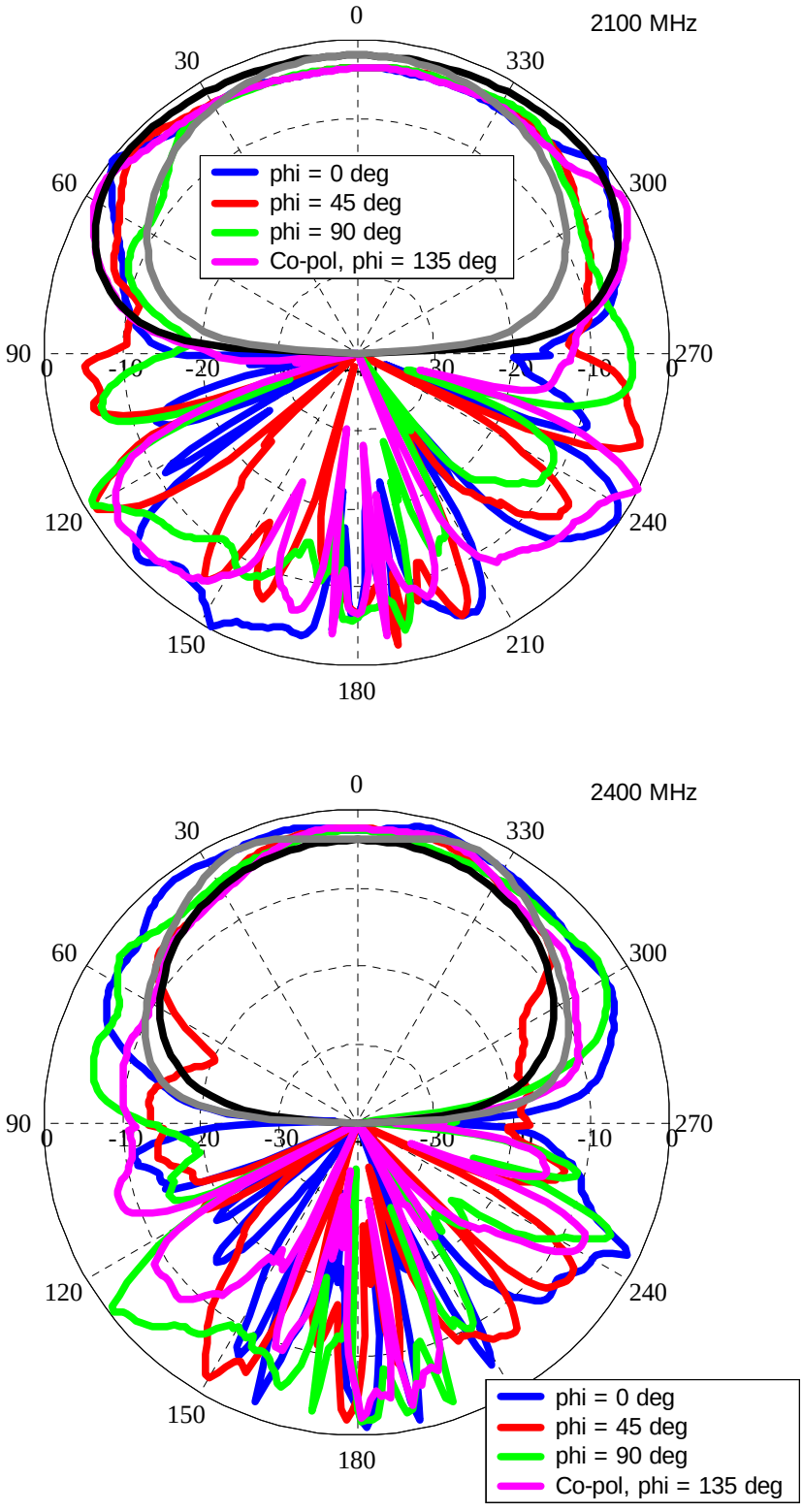

Figure 4.34 (cont) Measured star spiral axial ratio patterns of Fig. 4.27. Theta cuts. Black line is the simulated result for $\phi = 0°$ and the gray line is the simulated result for $\phi = 45°$.

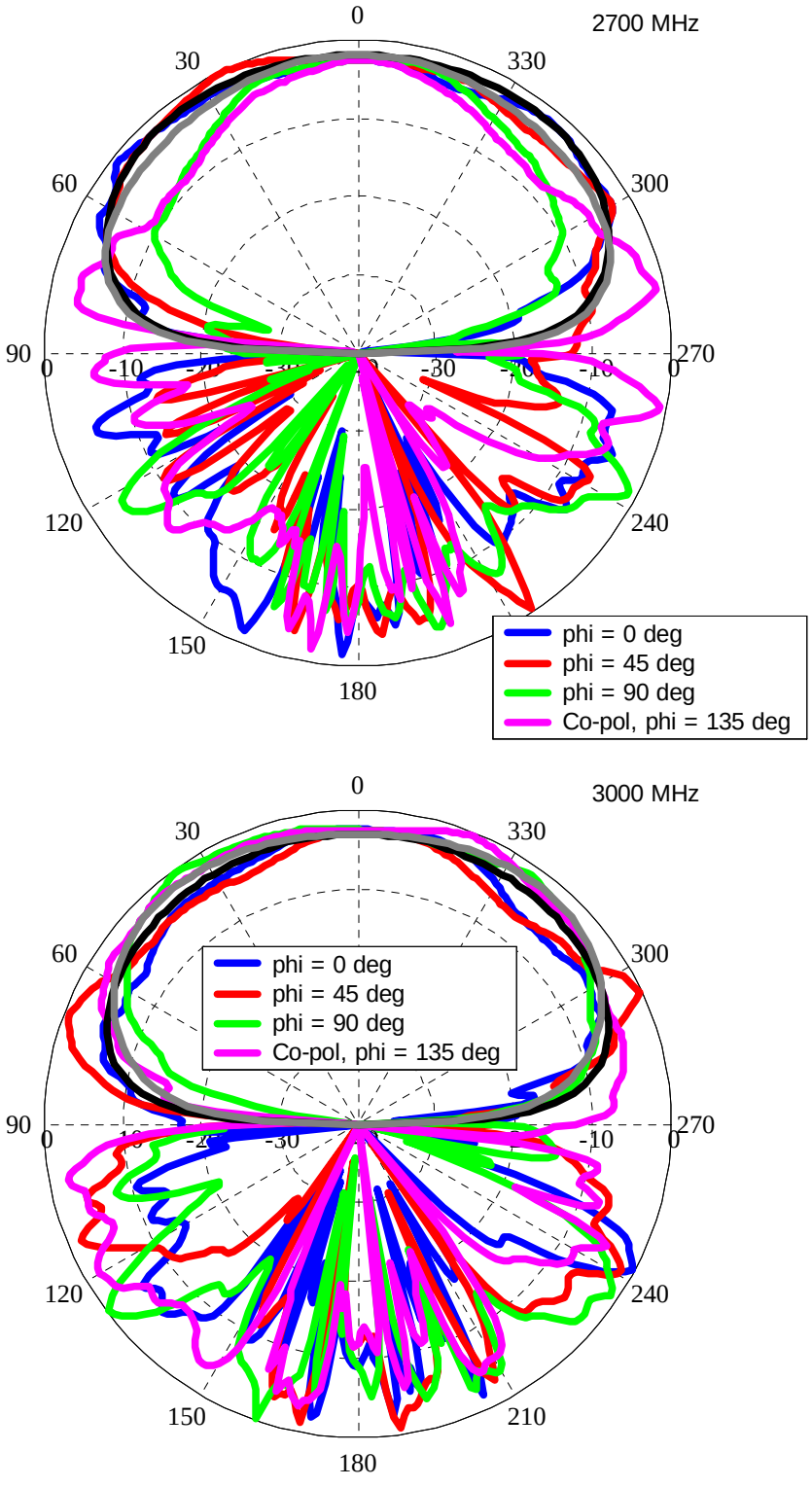

Figure 4.34 (cont) Measured star spiral axial ratio patterns of Fig. 4.27. Theta cuts. Black line is the simulated result for $\phi = 0°$ and the gray line is the simulated result for $\phi = 45°$.

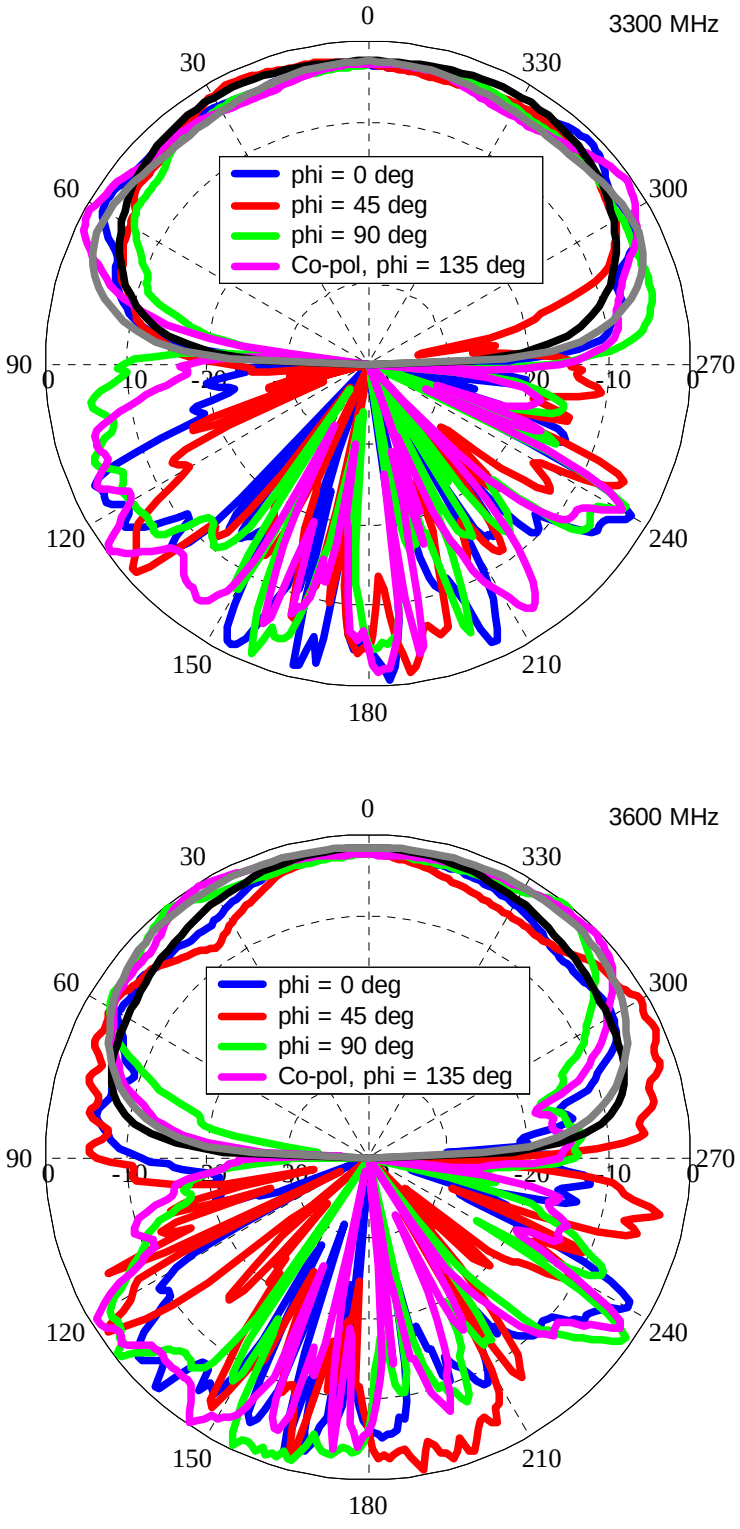

Figure 4.34 (cont) Measured star spiral axial ratio patterns of Fig. 4.27. Theta cuts. Black line is the simulated result for $\phi = 0°$ and the gray line is the simulated result for $\phi = 45°$.

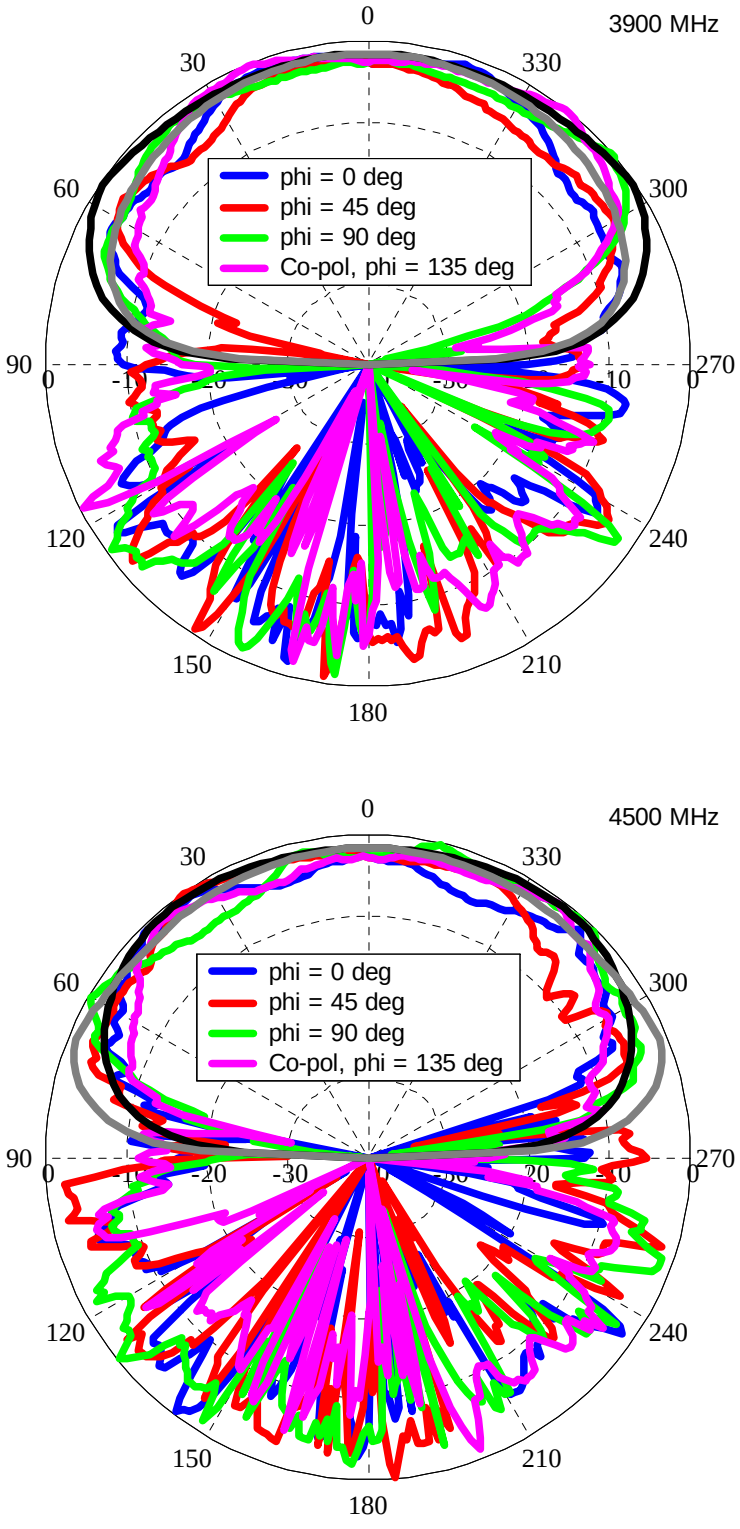

Figure 4.34 (cont) Measured star spiral axial ratio patterns of Fig. 4.27. Theta cuts. Black line is the simulated result for $\phi = 0°$ and the gray line is the simulated result for $\phi = 45°$.

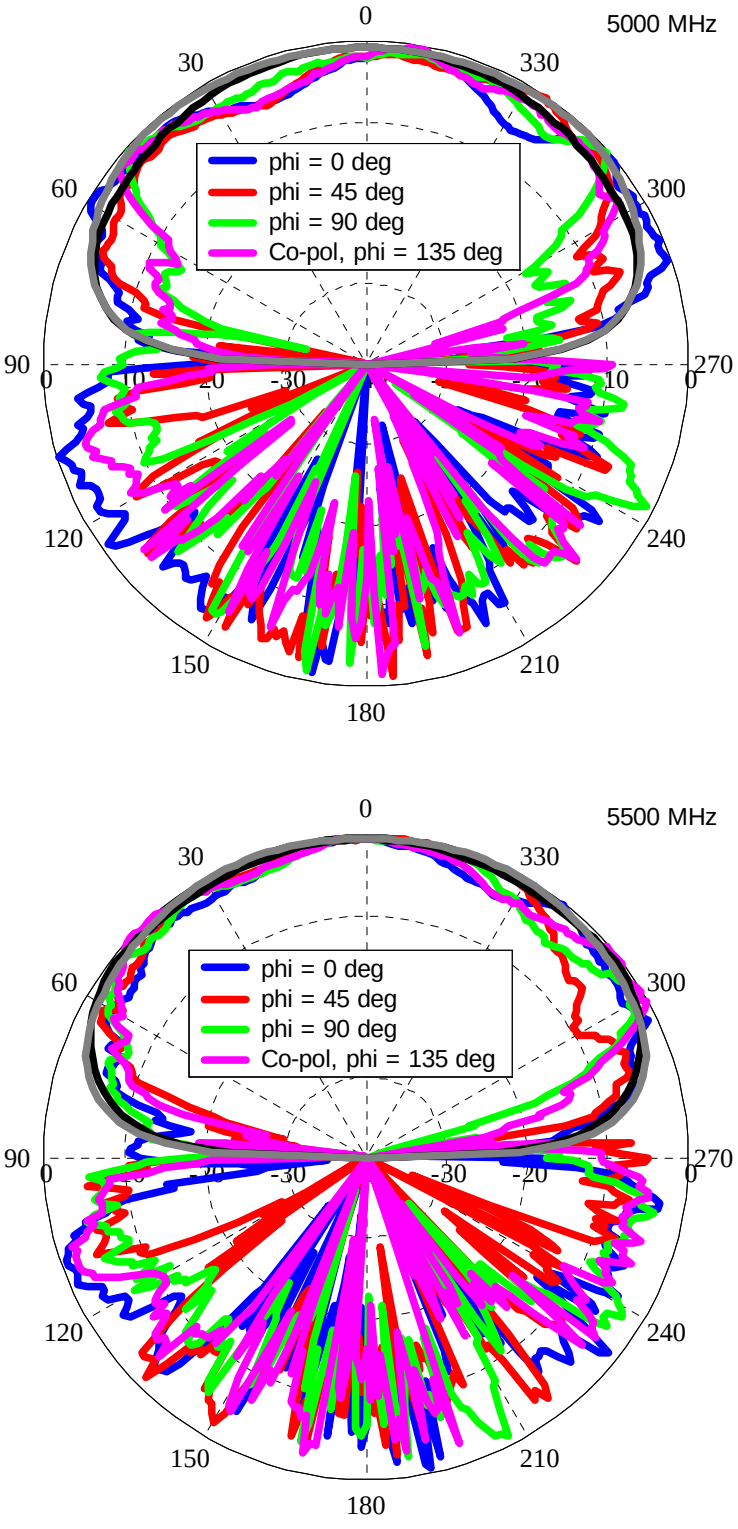

Figure 4.34 (cont) Measured star spiral axial ratio patterns of Fig. 4.27. Theta cuts. Black line is the simulated result for $\phi = 0°$ and the gray line is the simulated result for $\phi = 45°$.

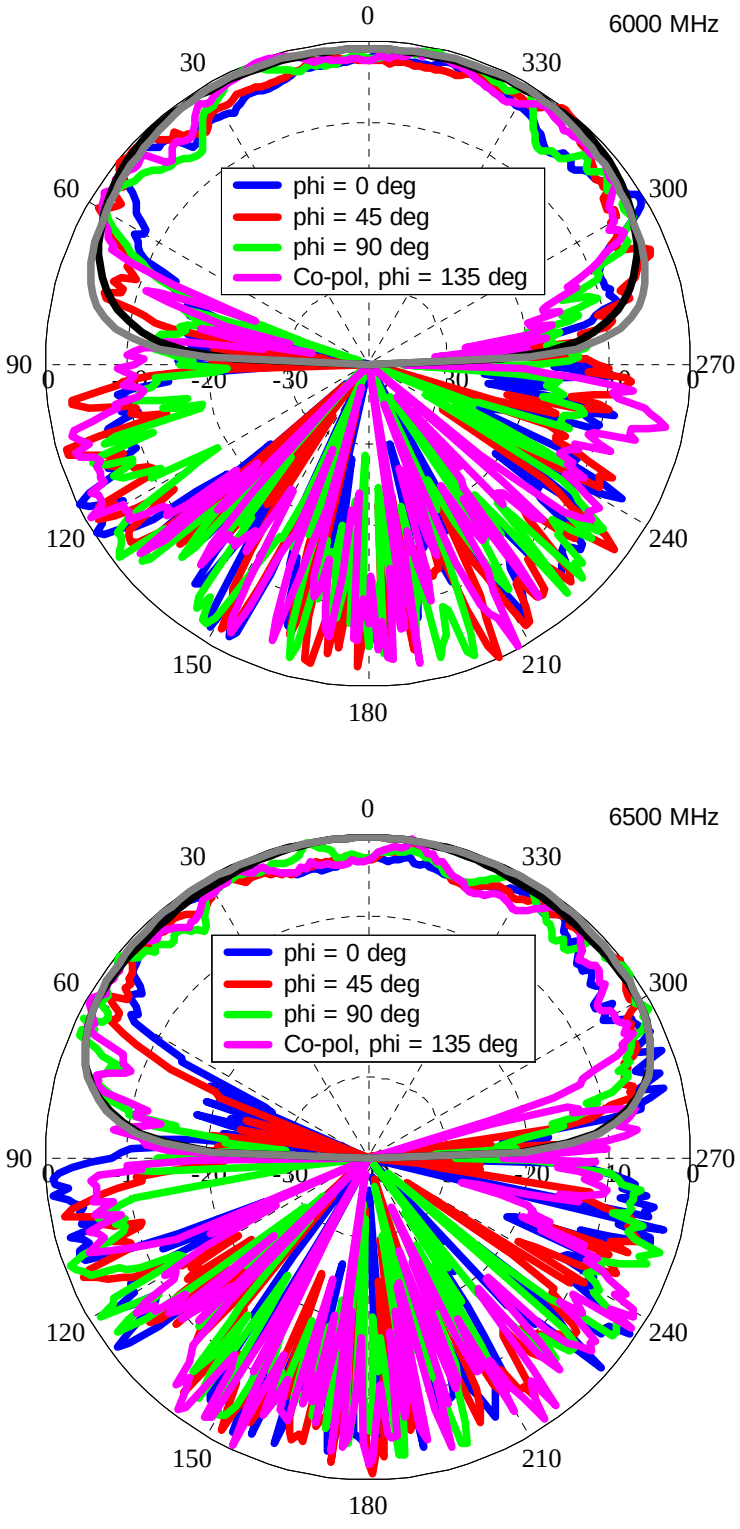

Figure 4.34 (cont) Measured star spiral axial ratio patterns of Fig. 4.27. Theta cuts. Black line is the simulated result for $\phi = 0°$ and the gray line is the simulated result for $\phi = 45°$.

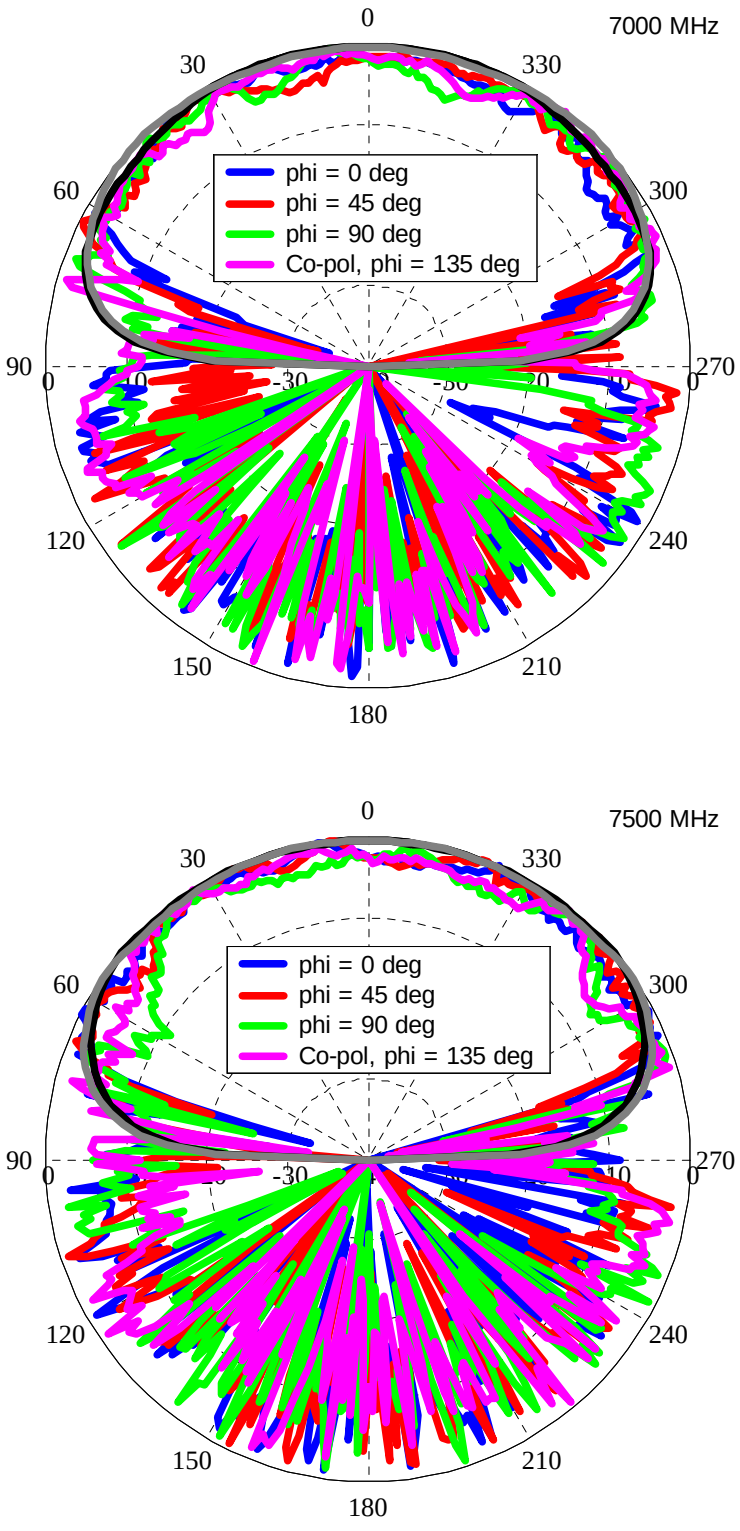

Figure 4.34 (cont) Measured star spiral axial ratio patterns of Fig. 4.27. Theta cuts. Black line is the simulated result for $\phi = 0°$ and the gray line is the simulated result for $\phi = 45°$.

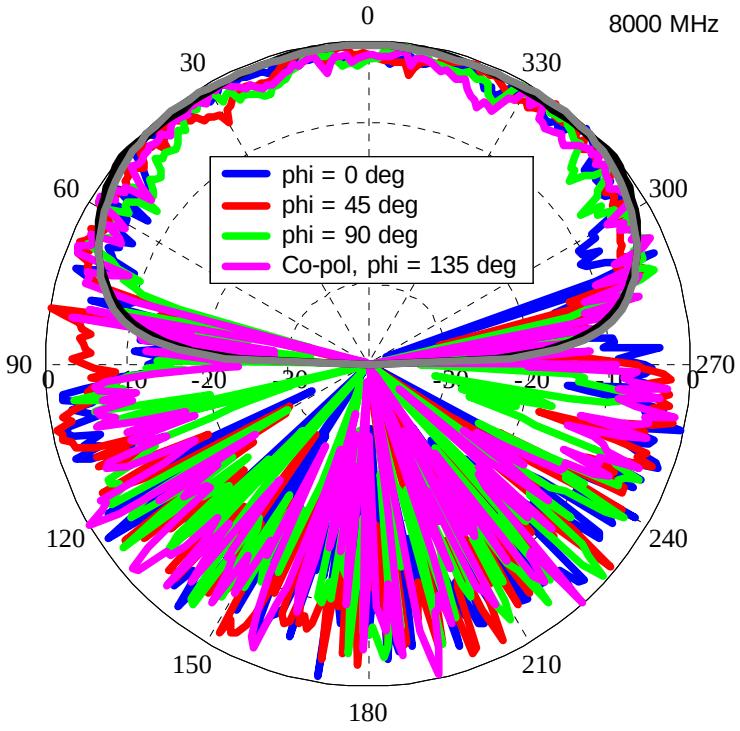

Figure 4.34 (cont) Measured star spiral axial ratio patterns of Fig. 4.27. Theta cuts. Black line is the simulated result for $\phi = 0°$ and the gray line is the simulated result for $\phi = 45°$.

4.5 Summary

A new type of slow-wave spiral antenna, the star spiral, has been introduced. The star spiral was optimized using the genetic algorithm to give a size reduction of 16.6% in simulations when compared to a circular Archimedean spiral. In simulation, the star spiral does not have quite as much size reduction as the square spiral but it offers other advantages. The star spiral is a more efficient antenna than the square spiral in terms of its low frequency cutoff when compared to its circumference. The ratio of size reduction to increased circumference, γ, for the star spiral is 0.88 compared to 0.69 for the square spiral. The star spiral also provides for unique array packing geometries that will be explored in the following chapters. The measurements and simulations of the star spiral show that the performance of the star spiral is very similar to the circular Archimedean spiral. The only significant drawback of the star spiral is its axial ratio performance at low frequencies, but this limitation can be overcome by using a 4-arm star spiral antenna when circular polarization is necessary.